SCUOLA DI DOTTORATO
UNIVERSITÀ DEGLI STUDI DI MILANO-BICOCCA

Department of Earth and Environmental Science
PhD program in Chemical, Geological and Environmental Sciences
XXXIII Cycle
Curriculum of Environmental Sciences

LARGE SCALE DRIVERS OF EXTREME PRECIPITATION VARIABILITY IN EUROPE

Candidate Mostafa Essam Abdelrahman HAMOUDA

Registration number 835506

Supervisor Prof. Claudia Pasquero

Coordinator Prof. Marco Malusà

ACADEMIC YEAR 2019/2020

UNIVERSITÁ DEGLI STUDI DI MILANO BICOCCA

Abstract

Department of Earth and Environmental Sciences

Doctor of Philosophy

LARGE SCALE DRIVERS OF EXTREME PRECIPITATION VARIABILITY IN EUROPE

by Mostafa Essam Abdelrahman HAMOUDA

European wintertime precipitation is known to be skilfully estimated in reanalysis data and model simulations since it is highly correlated with large scale, low frequency modes of variability, namely the North Atlantic Oscillation (NAO) and Arctic Oscillation (AO). Since the NAO and AO are mainly a wintertime mode of variability, the ability of estimating precipitation becomes more limited in the other seasons, most importantly in the summer, in which precipitation is mainly a result of mesoscale convection. The first part of the study uses observational data, reanalysis data, and the output of Weather Research and Forecast (WRF) model to study the recent changes of extreme daily precipitation events over Europe. It is found that in summer and transition seasons, more regions recorded an increase of extreme precipitation events than regions that recorded a decreasing trend. This is consistent with the global warming trends with Clausius-Clapeyron relation. The added value of using a high resolution, convection-permitting model to estimate precipitation extremes is deduced. The results show that WRF succeeds to correct the failure of ERA-Interim reanalysis to capture the positive trends of European extreme precipitation in summer and transition seasons that are indicated by the observational data (EOBS) and previous literature. On the other hand, more regions in Europe recorded negative extreme precipitation trends than regions with positive trends. This is found to be a consequence of the recent positive trend of the NAO over the past decades, causing more frequent positive NAO events, reducing extreme precipitation outbreaks to more

regions in Europe. As the NAO and the highly correlated AO are changing, further investigations to the nature of the two oscillations are carried out. Reanalysis data and climate model simulations of historical and warm climates are used to show that the relation between the two oscillations changes with climate warming. The two modes are currently highly correlated, as both are strongly influenced by the downward propagation of stratospheric polar vortex anomalies into the troposphere. However, when considering a very warm climate scenario, the hemispherically defined AO pattern shifts to reflect variability of the North Pacific storm track, while the regionally defined NAO pattern remains stable. The stratosphere remains an important precursor for NAO, and surface Eurasian and Aleutian pressure anomalies precede stratospheric anomalies. Idealized general circulation model simulations suggest that these modifications are linked to the stronger warming of the Pacific compared to the slower warming of the Atlantic Ocean, that is due to the slowdown of the Atlantic Meridional Overturning Circulation (AMOC).

Acknowledgements

I would like to express my appreciation to Professor Claudia Pasquero for generously supporting and supervising every single stage of this work. I learned a lot from her. She was always there, and never hesitated to offer any kind of support. For this and for many things, thank you very much! I really appreciate Professor Eli Tziperman for supervising a very big part of this thesis, and for inviting me to work with him in Harvard University. I learned a lot from him, and I appreciate the positivity and the optimism that he always provided. I am grateful for the University of Milano Bicocca for the opportunity. Thanks to Harvard University for the six months hospitality. Sincere thanks are also due to HPC-TRES grant 2017-03.

Special thanks to Luis Antonio for the friendship and the amazing times we spent together roaming around inside and outside Milano. It was always a great pleasure. Grazie al gruppo del terzo piano: Fabio, Vale, Giovanni, Bonali, Elena e Luca F, e anche ai miei amici in altri piani/edifici: Francesca B., Roberta P. Luca P. Ilaria. Grazie mille a Giulia B. per avermi mostrato la città di Como. Grazie mille anche a tutti coloro che mi hanno aiutato con l'italiano. I appreciate my residence friends Imiete, Hania. Thanks to my Trieste friends for the fun times: Vicharit, Adu, Tram, Hari, Youness. Thanks to Omar and Eslam, M.Basil, M.Yehia for the great times that we spent together remotely. Thanks to Ahmed Elezaby and Rodrigo V. for being there remotely. Grazie a Chiara D., Agostino, Anna, Fabien, Alice. E' stato divertente condividere tutto con voi.

My heartfelt thanks to my fiancée Radwa, without whom the end of the PhD would not have been as happy as it was! Thank you for the love and support!

Finally, I would like to express my warmest gratitude and appreciation to my family: Mom, Dad, Mahmood, Rehab and Rabab for always being there for me during the tough and happy times. Thank you for the unconditional love and continuous support!

Contents

List of Figures

. . .

Chapter 1

Introduction

1.1 Background

The dynamical and thermal features arising from solar differential heating over the globe are characterized by rising air in the low pressure band around the equator due to strong heating, known as the Intertropical Convergence Zone (ITCZ). By the principle of continuity in fluid dynamics, and accounting for Earth's rotation, subsidence of air occurs in the subtropics around $25^\circ - 30^\circ$, creating what is known as the subtropical high pressure. The subsiding air splits up on the surface into two directions: southward flow closing the so-called Hadley Cell, and northward flow colliding with the return flow from the pole causing another convergence zone known as the polar front, closing both Ferrel and Polar Cell (Figure 1.1).

Accounting for the non-uniformity of Earth's surface, the distribution of land and ocean masses modifies the previously described idealized circulation model. Mid-latitude mean winter climatological pattern is characterized by several well-known features. From air-mass

distribution point of view, the climatology of atmospheric pressure at sea level is characterized by the following: two high pressure centers over the freezing cold land masses, known as: Siberian high, and Canadian/North American high, extending to the Azores; two low pressure centers over the relatively warm oceans, known as the Icelandic low over the North Atlantic ocean, and the Aleutian low over the Pacific ocean. An adjoining high pressure center persists over the polar cap (Figure 1.2).

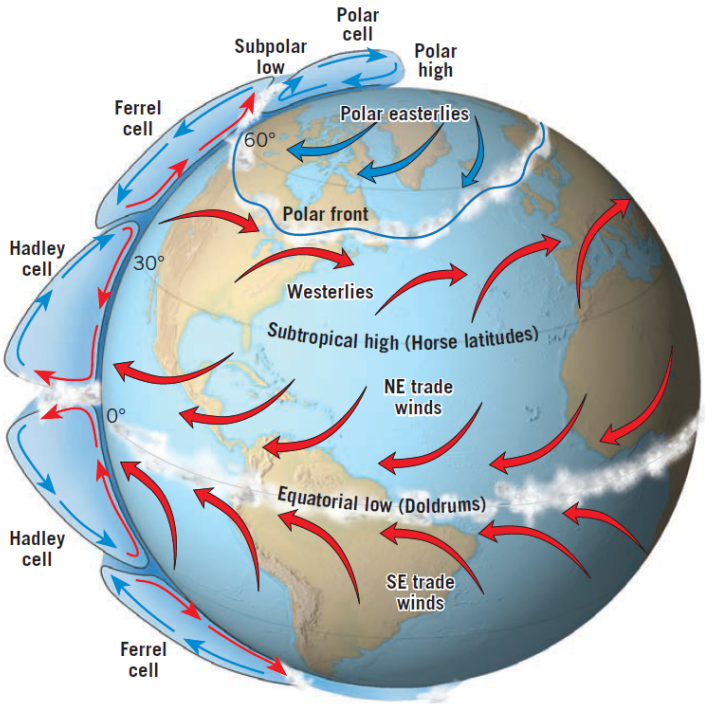

FIGURE 1.1: Idealized global circulation for the three-cell circulation model on a rotating Earth (From Lutgens and Tarbuck (2016)).

The sharp gradient between the warm air mass in the subtropics and the cold air mass in the pole is in dynamical equlibrium with westerly

geostrophic wind, which is basically a balance of two opposite forces: pressure gradient force (due two differential heating) and Coriolis force (due to Earth's rotation). The resulting westerlies are even more intensified by the thermal wind relation in the upper levels due to different thickness of atmospheric columns in the warm and cold air masses in a narrow region. This intensification causes the Jet stream, which is a strong westerly wind in the upper level around 100-200 hPa height.

The thermal wind V_T is the vertical derivative of the horizontal wind that is the rate of change of the geostrophic wind ($\mathbf{V_g}$) with respect to pressure ($\ln p$), and is given by (Holton, 2013):

$$\frac{\partial \mathbf{V_g}}{\partial \ln p} = -\frac{R}{f}\mathbf{k} \times \nabla_{\mathbf{p}} T \tag{1.1}$$

$$V_T(p) = \frac{1}{f}\mathbf{k} \times \nabla \left(\Phi_1 - \Phi_0\right) = \frac{R}{f} \ln\left(\frac{p_0}{p}\right) \mathbf{k} \times \nabla \bar{T} \tag{1.2}$$

where f is Coriolis parameter, Φ is geopotential height at isobaric surface, R is gas constant, $\bar{T}$ is average temperature between pressure level p and p_0. A similar stream is found further high above the surface at the Stratosphere, named the Stratospheric Polar Vortex, which is the main dynamical feature of this layer of the atmosphere. It is a circulation of fast moving cyclonic air over the Arctic. In winter, the stratospheric polar vortex is mainly strong, with wind speeds over $200 km/h$, confining the freezing air of the Arctic. However, for several reasons, some disruptions may occur to this steadily moving flow, forcing it to weaken, and therefore meander.

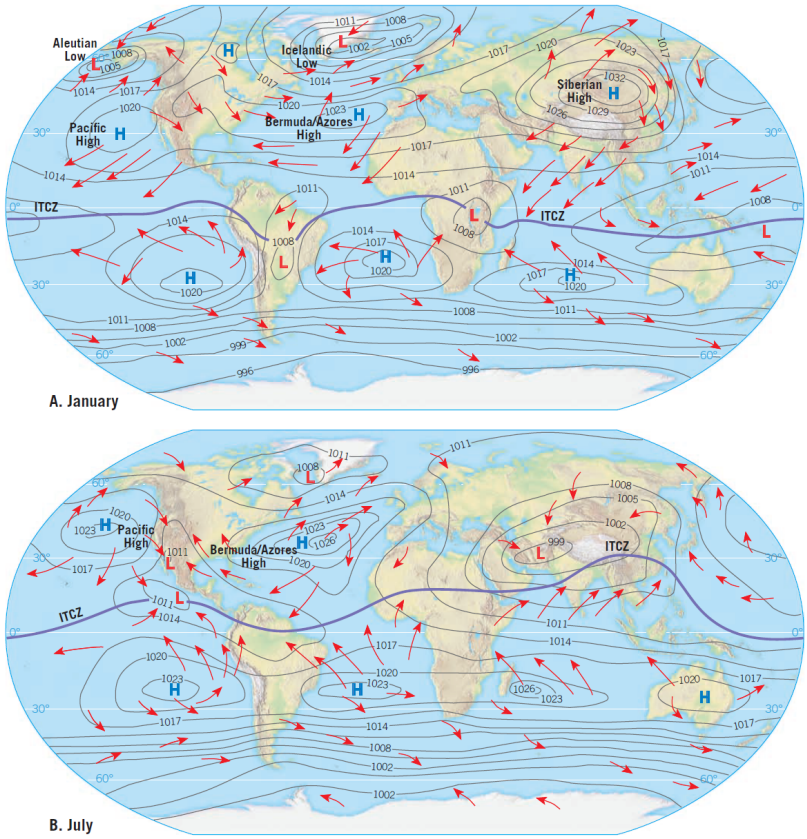

FIGURE 1.2: Average surface pressure and associated global circulation for A) January, B) July. Contour unit: hPa. (From Lutgens and Tarbuck (2016)).

A weakening of the polar vortex is an important wintertime phenomenon, since it is associated with extreme weather events over the mid-latitudes, such as snowing and extreme floods. An example of a polar vortex weakening is the extremely cold winter of 2018 over North America and Europe (Overland et al., 2020), in which Arctic freezing air advection penetrated south causing snow fall as far as Rome. On

contrary, an example of an extremely strong polar vortex in late winter of 2020 is discussed by Lawrence et al. (2020), showing how constrained the polar cold air mass around the Arctic, resulting in average winter conditions. This correlation between surface level weather conditions and 30-km high polar vortex is know as the Stratosphere-Troposphere interaction. Baldwin and Dunkerton (2001) explains how a weakening of the polar vortex result in a change of surface pressure distribution and storm tracks in the mid-latitudes. It was found that stratospheric polar vortex anomalies are accompanied by cold air spells in the mid-latitude by modifying the aforementioned pressure centers. A weak polar vortex causes the jet stream to meander, bringing cold air masses from the Arctic southwards to the mid-latitude, and warm air masses from the mid-latitudes to the polar region. This mass redistribution projects on the two phases of the Arctic Oscillation (AO) mode of variability. A positive (negative) phase of AO translates into positive (negative) anomalies of Azores and Aleutian pressure centers, and negative (positive) anomalies of the Arctic pressure center. The covariance between the three pressure centers is correlated with the stratospheric polar vortex, where a strong (weak) polar vortex is associated with a positive (negative) AO phase. Another similar covariance pattern is the North Atlantic Oscillation (NAO), which is a local manifestation of the AO, only in the Atlantic region, consisting of the Icelandic and the Azores pressure centers. Similarly, a positive (negative) NAO reflects negative (positive) anomalies over the Icelandic pressure center and positive (negative) anomalies over the Azores pressure center.

As a result, wintertime precipitation over North America and Europe are mainly controlled by the large-scale oscillating pressure systems. For instance, when the NAO is in a positive (negative) phase, storm tracks drive mid-latitude depressions towards northern (southern) Europe, resulting in dry (wet) conditions in southern (northern) Europe, and wet (dry) conditions in northern (southern) Europe.

Moving to the summertime of the year, the dynamics of the circulation in the mid-latitudes change substantially. Strong heating over land masses causes the air to ascend, inducing thermal low pressure areas. While over the oceans, the subtropical highs strengthen as the oceans are relatively cooler than the continents. These high pressure centers drive moist air into the continents, to compensate by continuity for the thermal lows. Under certain conditions, this process is very important for a very large portion of precipitation in the summer, by which more than 70% of the total precipitation over Europe and North America is a result of mesoscale convection (Eshel and Farrell, 2001).

Consider a moist air parcel with the temperature and specific humidity properties as in the figure 1.3. This parcel under normal conditions is stable. However, the air parcel can be lifted by several mechanisms such as: flowing over orography or surface convergence due to low pressure perturbation (such as land-sea breeze heat lows). This upward motion reduces parcel's temperature following the dry adiabatic lapse rate DALR ($9.8°C/km$), which is the rate by which the air cools down when lifted vertically in the atmosphere conserving its moisture content. Once the temperature of the parcel (T_p) is reduced enough to equal its dew-point temperature (T_d), condensation starts at what is

called the Lifting Condensation Level (LCL). If the temperature of the surrounding air (environmental air temperature T_{env}) is lower than the lifted air parcel, the air parcel is positively buoyant and will continue its ascent. However, if T_{env} is higher than the lifted air parcel, this renders the parcel negatively buoyant. This negative buoyancy can be overcome if the parcel has enough momentum or energy supply that is proportional to this inhibition barrier by negative buoyancy (Convective Inhibition CIN). In this case, the parcel continues to ascend reaching the Level of Free Convection (LFC), after which the parcel is lifted by positive buoyancy force and condenses its moisture by further temperature reduction following the moist adiabatic lapse rate (around $5°C/km$, that is lower than DALR, since latent heat released by condensation slows down cooling rate). The positive buoyancy translates into energy that is enough to lift the parcel autonomously high up in the atmosphere, and is known as the Convective Available Potential Energy (CAPE). This process continues until the environmental temperature is warmer than parcel's temperature, causing buoyancy force to become neutral (Level of Neutral Buoyancy LNB).

Unlike large scale fronts, it should be noted that such mechanism can occur on very small scale (less than $10km$). For example, under the condition of strong heating over a certain region, the air parcel can be heated up to the Convective Trigger Temperature (assuming constant or increasing moisture content), at which the air parcel becomes positively buoyant and overcomes Convective inhibition. The convective triggering temperature is relevant when convection is not mechanically

forced, but rather a consequence of diurnal heating. If the soil conditions are wet, heating induces a flux of moisture, that makes the parcel even less dense, and reduces the convective trigger temperature (Taylor, 1997).

Relevantly, temperature and moisture are two tied physical parameters by the Clausius-Clapyeron equation, which states that: the air parcel at high temperature can hold more moisture than an air parcel at lower temperature. This relation is given by equation 1.3 (Ambaum, 2010):

$$e_s = e_{s0} \exp\left[\frac{L_v}{R_v}\left(\frac{1}{T_0} - \frac{1}{T}\right)\right] \tag{1.3}$$

where e_s is saturation vapor pressure at temperature T. e_{s0} is saturation vapor pressure at temperature T_0. L_v is specific latent heat, R_v is gas constant for water vapor. Saturation vapor pressure is also given empirically by Bolton's formula in equation 1.4

$$e_s(Pa) = 611.2 \exp\left(\frac{17.67T(^\circ C)}{T(^\circ C) + 243.5}\right) \tag{1.4}$$

Note that the exponential dependence of vapor pressure on temperature has important consequences on the mixing of air parcels, causing two unsaturated air parcels to become oversaturated after mixing, and thus is relevant for processes such as atmospheric convection.

Temperature-moisture relation becomes even more relevant considering global warming. When global temperature increases, the air can hold more moisture, hence more precipitation. This increase in precipitation is reflected in increasing frequency and intensity of extreme

events in the recent decades (IPCC, 2013; Papalexiou and Montanari, 2019), where studies show that there are more regions in which extreme precipitation events are increasing than decreasing. In summer, extreme precipitation due to convection becomes more relevant, especially when considering the increasing moisture supply from warming sea surface due to global warming (Rahmstorf et al., 2015). In winter, mean and extreme precipitation are correlated to AO and NAO (Hurrell, 1995; Thompson and Wallace, 1998; Scaife et al., 2008; Casanueva et al., 2014). Extreme weather outbreaks in the midlatitude are also related to the relatively faster rate of warming in the arctic region with respect to low latitudes (Cohen et al., 2014) known as the Arctic Amplification, which is partly due to Ice-Albedo feedback mechanism, whereby the loss of sea ice reduces surface Albedo, consequently more warming that leads to more sea ice loss.

All of the previous physical and dynamical processes are well documented and described using mathematical equations. These equations are implemented together, and solved in Climate Models to simulate the real world as close as possible. General Circulation Models (GCMs) use mathematical equations to characterize how energy and matter interact in different parts of the ocean, atmosphere, land. Building and running a climate model is complex process of identifying and quantifying Earth system processes, representing them with mathematical equations, setting variables to represent initial conditions and subsequent changes in climate forcing, and repeatedly solving the equations using powerful supercomputers.

Climate projections under the influence of greenhouse gas emissions

become an issue that could be tackled using climate models, and therefore, provide ideas on how a hypothetical emission scenario could affect the current climate. The Representative Concentration Pathways (RCP) is a convention for greenhouse gas (GHG) trajectories as adopted by IPCC (2013). The trajectories describe different climate futures, based on different possibilities of radiative forcing due to the emission of GHGs.

In this study, models are exploited to cover some gaps in our understanding of the climate system. It is not fully understood how large-scale atmospheric variability patterns drive extreme precipitation variability. The complex interaction of the large-scale stratospheric polar vortex, with the tropospheric synoptic patterns is important to be understood as it influences winter weather. Uncertainties in seasonal and sub-seasonal forecast arise from the low skill in predicting drivers of Stratospheric Polar Vortex. Further uncertainties arise in extreme precipitation variability due to the lack of observational data in some regions. Therefore, the need to use climate models arises to solve large scale and small scale dynamics

The goal of this thesis is to investigate the recent trends in extreme precipitation frequency and intensity on the mesoscale, focusing on the added value of using convection resolving models at high resolution to quantify precipitation extremes, shedding light on the recent trends of the North Atlantic Oscillation and its impact on the reduction of winter precipitation extremes over Europe. Moving over to the synoptic scale, it is aimed to advance the understanding of the nature of the coupling between AO and NAO given the climate mean state changes under global warming, and how stratosphere-troposphere coupling is an

important component, connecting the Pacific and the Atlantic oceans.

1.2 Outline

The relevant literature is given in the beginning of each chapter. Methods, results, discussion and conclusion follow afterwards. In chapter 2, the objective is to study how extreme precipitation frequency and intensity have been changing in the recent decades, focusing on how resolving mesoscale convection processes is important to better represent precipitation extremes, most importantly in summer. In winter, a special focus on the recent changes regarding the main driver of the mean and extreme precipitation (i.e. NAO), and how it is related to a declining trend of winter precipitation extremes over Europe. Chapter 3 is dedicated to study the nature of the coupling between AO and NAO in light of stratosphere-troposphere interactions. The chapter answers why the AO and NAO are strongly coupled, how to break this coupling, what are the consequences on stratosphere-troposphere coupling, and how the Atlantic and the Pacific ocean temperatures play an important role in regulating atmospheric variability in the mid-latitudes. Finally, general conclusions are presented in chapter 4.

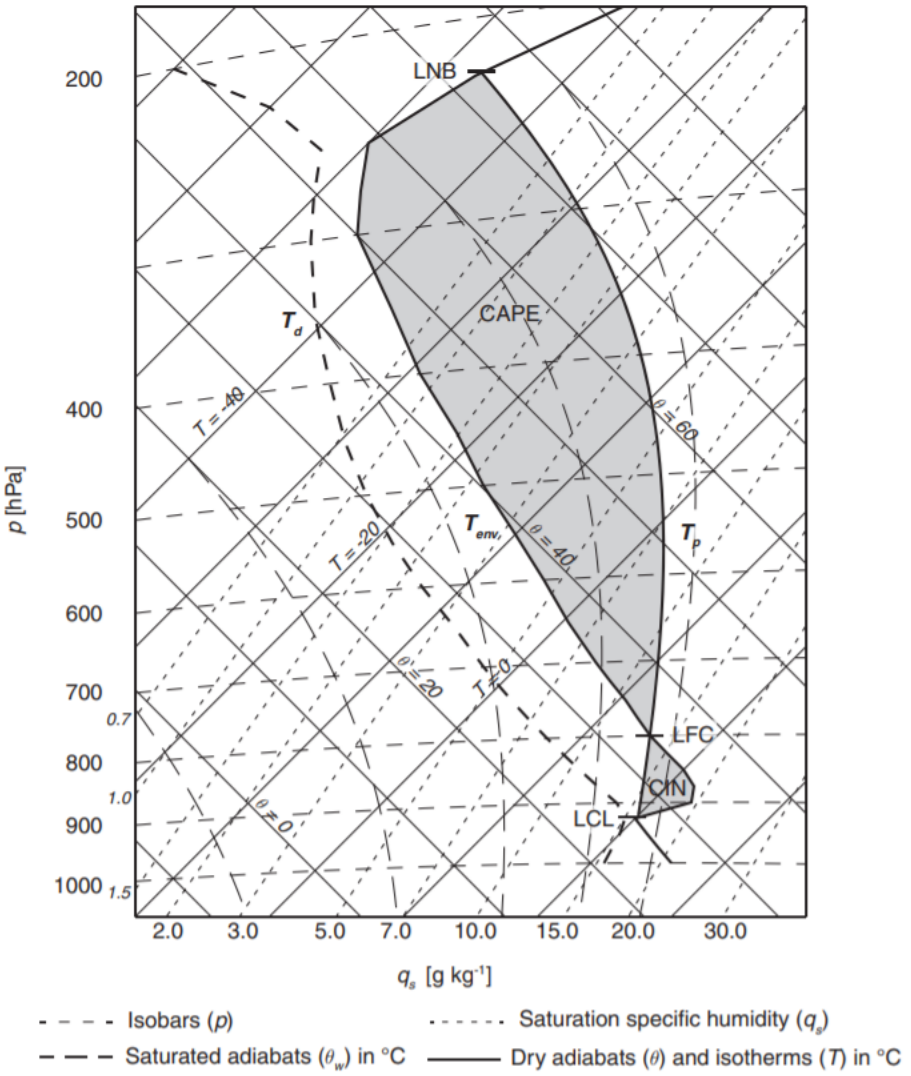

FIGURE 1.3: Tephigram (Skew T-LogP) including examples of the LCL, LFC, LNB, CAPE and CIN for a given atmospheric temperature profile T_{env} (bold solid line) and dew point profile T_d (bold broken line). (From Lohmann (2016)).

Chapter 2

Recent Extreme Precipitation Trends over Europe

2.1 Introduction

* One of the most discussed effects of the current climate crisis is the change in the occurrence of extreme precipitation (Trenberth, 2011; Trenberth and Josey, 2007). Considering the rarity and the spatial heterogeneity of the events (Myhre et al., 2019), the determination of the existence of statistically significant trends is very challenging. A very large number of multidecadal time series is necessary to address the issue. Nevertheless, in the scientific community there is a growing consensus on the fact that there are more regions in which heavy precipitation is increasing than decreasing (IPCC, 2013; Papalexiou and Montanari, 2019; Seneviratne et al., 2012). The use of models and reanalysis data

*The contents of this chapter are mostly submitted for peer review in the article: **Hamouda M.E., Pasquero C.. European Extreme Precipitation: the effects of spatio-temporal resolution of the data.** 1st round of review, Weather and Climate Extremes Journal

to support the observed trends is limited by their relatively low spatial resolution, especially considering that long simulations are required.

In some cases, observations have shown that heavy precipitation is correlated with large scale variability patterns, a link that is also well represented in models. One of the most studied links is that between European precipitations and the North Atlantic Oscillations (NAO) (Hurrell, 1995; Walker and Bliss, 1932; Thompson and Wallace, 1998; Deser, 2000; Totz et al., 2017; Gueremy, Laanaia, and Ceron, 2012). The NAO is an alternation of high and low pressure anomalies between Icelandic and Azores pressure centers. A positive NAO phase means low pressure anomalies in the Icelandic pressure center, and high pressure anomalies in the Azores pressure center, resulting in wet conditions over Northern Europe, and dry conditions over Southern Europe, and vice versa for a negative NAO phase. And studies have shown that both mean precipitation and the occurrence of extreme precipitation events in Europe in the winter season are mainly influenced by the phase of the NAO (Scaife et al., 2008; Cohen et al., 2014; Casanueva et al., 2014).

As the NAO is mainly a wintertime mode of variability, the skill of models to reproduce seasonal precipitations becomes significantly lower in the other seasons, most importantly in summer (Casanueva et al., 2014), when rainfall is mainly a result of convection. A good representation of the convective scales requires the use of a high resolution, convection-permitting model, as model physics and parameterizations play an important role in precipitation downscaling (Dereczynski et al., 2020), especially in complex orography regions (Giorgi et al., 2016). For

example, it has been shown that summertime precipitation is highly underestimated in Europe using CMIP5 models (Huang et al., 2017), and over the UK using ERA-Interim reanalysis data (Leeuw, Methven, and Blackburn, 2014). ERA-Interim is known to have lower frequencies of extreme precipitation events due to its low spatial resolution (Skok et al., 2015), and summer extreme precipitation trends in Europe are also characterized by spatial variability that can have opposite signs in close regions (Zolina et al., 2005; Zolina et al., 2008). For these reasons, the use of high resolution, convection-permitting models is a promising approach to have an added value for a better quantification of precipitation.

In this study, the dynamical downscaling of ERA-Interim reanalysis is adopted using the high resolution Weather Research and Forecast (WRF) model for a period of 30 years, to analyze extreme precipitation at high spatial and temporal frequencies (4 km grid spacing, 3-hourly accumulated precipitation), to compare their interannual variability and trends with observational and reanalysis data. Data and methods are in section 3.2, and in section 2.3 the results are discussed.

2.2 Data and Methods

2.2.1 Data

The daily observational dataset is obtained from the EU-FP6 project UERRA (https://www.uerra.eu) and the Copernicus Climate Change

Service, named E-OBS. It is constructed through a conditional simulation procedure interpolating station-derived meteorological observations, and comes as an ensemble dataset available on a 0.1 and 0.25 degree regular grid starting from 1950. In this study, the 0.1 degree ensemble is used from the period 1979 to 2008 which is the period that overlaps with the high resolution WRF simulations. In this study, this dataset is taken as the "truth" as it is derived from meteorological stations. More details about EOBS construction are found in (Cornes et al., 2018).

Reanalysis data is obtained from the European Centre for Medium-Range Weather Forecasts (ECMWF) ERA-Interim (Dee et al., 2011) for precipitation and sea level pressure, in the period from 1979 to 2008. The spatial resolution is 80 km. The most recent reanalysis data ERA5 is also used, for the same period, with spatial resolution of about 31 km (Hersbach et al., 2020).

For the high resolution model data, the output of the simulation run by Institute of Atmospheric Sciences and Climate - CNR using the Weather Research and Forecasting (WRF) model is adopted. The simulation is forced by ERA-Interim reanalysis from 1979 to 2008, downscaled to a spatial resolution of 4 km over the EUROCORDEX domain, and the 3-hourly temporal resolution. The simulation was validated by comparing precipitation climatology with various observational data such as EOBS, CRU and GPCC (Pieri et al., 2015). It was found that WRF 4 km simulation has a lower bias with respect to EOBS data, compared with ERA-Interim reanalysis, specifically in the summer season JJA. Over the European domain, the percentage differences of WRF 4

km to EOBS is 17%, while it is 21% for ERA-Interim to EOBS. Moreover, in the Great Alpine Region, the percentage difference between WRF 4 km and HISTALP (Historical Instrumental Climatological Surface Time Series Of The Greater Alpine Region) dataset is only 3%. In general, WRF 4 km simulation tends to perform exceptionally well in summer. An overestimation of the average rainfall is however found in winter season. On the other hand, ERA-Interim overestimates summer precipitation, while it is more accurate in winter precipitation. More details about the simulations and the validation are found in (Pieri et al., 2015).

2.2.2 Methods

The North Atlantic Oscillation is defined in (Hurrell and Deser, 2009) by calculating the leading mode of the Empirical Orthogonal Function (EOF) (see section 3.2.3) for sea level pressure anomalies obtained from ERA-Interim reanalysis, for the domain $(90°W - 40°E, 20°N - 80°N)$. Monthly data of December, January, and February (DJF) are considered. The linear trend of the period from 1979 to 2008 is removed, and the dataset is weighted by the square root of cosine of latitude (North et al., 1982), then the covariance matrix is computed.

To estimate the 95th percentile of precipitation at each grid point, the procedure described in (Husak, Michaelsen, and Funk, 2007; Zolina et al., 2009) is used. First, a distribution function is obtained using the whole (daily or three hourly) time series. Then, a gamma distribution $\Gamma(x, \alpha, \beta)$ is fitted to the distribution function using shape parameter α and scale parameter β. To obtain α and β, let x be precipitation time

series with length n_p:

$$A = \ln(\bar{x}) - \frac{\sum_i^{n_p} \ln(x_i)}{n_p} \tag{2.1}$$

$$\alpha = \frac{1}{4A}(1 + \sqrt{1 + \frac{4A}{3}}) \tag{2.2}$$

$$\beta = \frac{\bar{x}}{\alpha} \tag{2.3}$$

Once the Gamma distribution is defined at each grid point, the corresponding 95th percentile threshold is obtained from the Gamma Cumulative Distribution Function. A sample of fitting Gamma probability distribution function to the probability distribution of observed precipitation data from ERA-Interim is shown in figure 2.1. The figure shows the probability distribution function for the region ($9°E \pm 3°, 45°N \pm 3°$) and the fitted Gamma distribution, which becomes more accurate when representing more extreme values of precipitation.

The interannual variability of extreme precipitation is then estimated following the procedure described in (Papalexiou and Montanari, 2019): the top 2.5% most extreme precipitation events are recorded over the 30 years of study. Then, a yearly time series of frequency of occurrence and accumulated intensity of extreme precipitation is obtained. The effects of the choice of the percentile of events studied was tested using 1.25%, 2.5%, 5%, and has no substantial influence on the conclusions.

To examine the effect of grid resolution on extreme precipitation trends, WRF 4 km simulation is upscaled to match ERA-Interim grid

resolution. Using First-order Conservative Remapping (Jones, 1999), WRF 4 km curvilinear grid was remapped to ERA-Interim longitude-latitude grid with a resolution of 80 km.

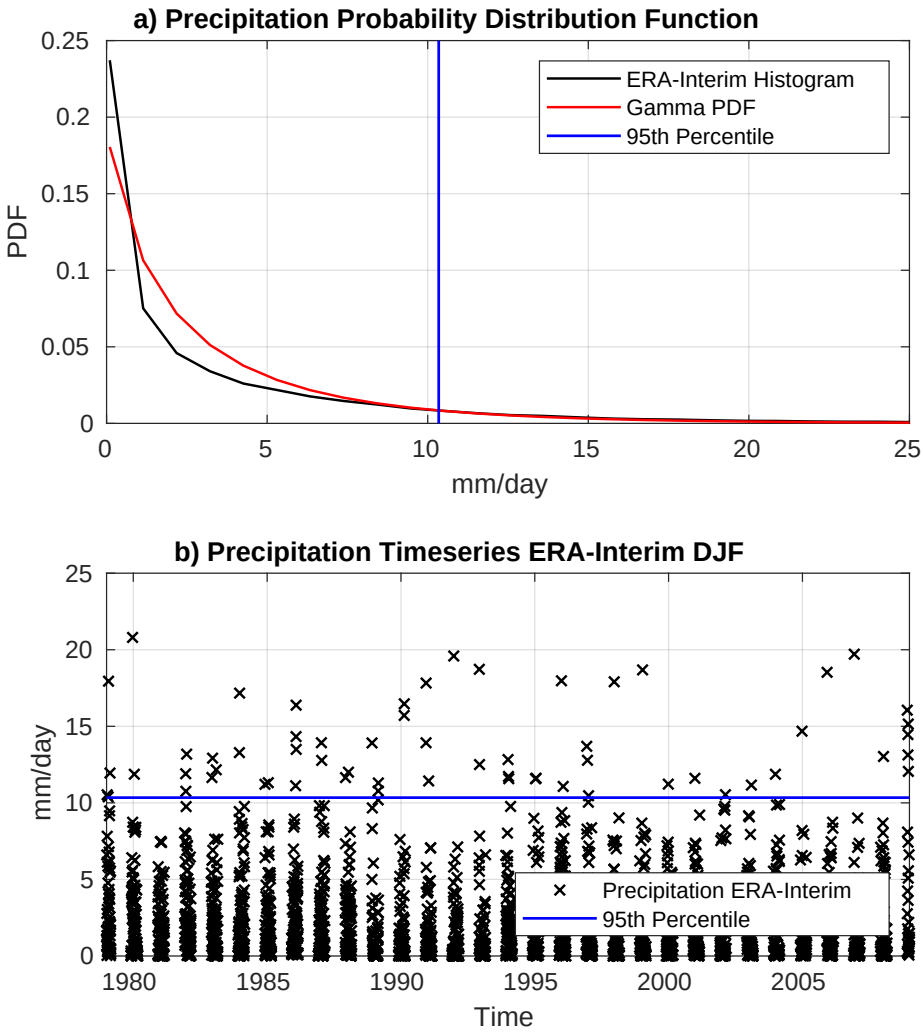

FIGURE 2.1: a) An example of the probability distribution function of the observed precipitation data of ERA-Interim reanalysis in winter season (DJF) for the region ($9°E \pm 3°, 45°N \pm 3°$) (black), and the corresponding Gamma probability distribution function (red), with the 95th percentile threshold marked in (blue). b) Daily timeseries of wintertime ERA-Interim precipitation that is used to obtain the distribution function in (a), with the 95th percentile threshold marked by the blue line.

2.3 Results and Discussion

2.3.1 Extreme precipitation threshold

Extreme precipitation threshold is defined as mentioned in section 3.2 by fitting a Gamma distribution function to precipitation distribution function at each location, and identifying the corresponding 95th percentile value of the Gamma distribution.

Figures (2.2, 2.3) show maps of the 95th percentile threshold of seasonal precipitation for EOBS, ERA-Interim reanalysis, and its high resolution dynamical downscaling using WRF for daily and 3-hourly time scales. The figures show that the patterns of the 95th percentile are in good agreement in the different seasons for the four datasets, where a higher extreme thresholds follow coastlines and high orography regions.

The high resolution data accommodates more detailed structures of extremes' threshold, particularly in regions with high orography (i.e. the Great Alpine Region). The different amplitudes of the 95th percentile between low resolution reanalysis and higher resolution EOBS and WRF is owed to the spatial averaging in the low resolution grid box in ERA-Interim. Therefore, the high resolution downscaling is crucial for an accurate definition of the extreme precipitation at a given location.

The differences between the daily and 3 hourly accumulated precipitation in high resolution WRF output have a seasonal pattern: the

95% threshold is typically larger for daily values, except for the summer season. This can be rationalized as short-duration summer precipitation is typically a result of intense convective events. Consistent with (Hodnebrog et al., 2019), sub-daily extreme precipitation pattern differs from that of the daily pattern, in which higher extreme value is indicated in the 3-hourly WRF simulation. This can be seen by comparing figures 2.3(b,f), where 3-hourly summer precipitation has generally threshold than that of the daily.

2.3.2 Large Scale Synoptic Variability

Many studies show how the North Atlantic Oscillation drives wintertime mean precipitation in Europe (e.g. Hurrell (1995) and Hurrell and Deser (2009)). Here it is show that not only mean rainfall is correlated with the NAO, but also the extreme precipitation is affected by the NAO phase (consistent with Casanueva et al. (2014)). Figure 2.4,2.5 show the temporal correlation of the monthly accumulated precipitation exceeding the 95th percentiles (shown in figures 2.2,2.3) with the NAO index, for each season. Only significant correlations ($p - value < 0.05$) are shown. For wintertime extreme precipitation, the figures show the well known dipole-like correlation, in which northern Europe is correlated to NAO, while southern Europe is anti-correlated to NAO. Summer NAO negative correlation with extreme precipitation is seen in limited areas in northern Europe, and unlike in (Casanueva et al., 2014), the positive correlation disappears in southern Europe for this 30-year period.

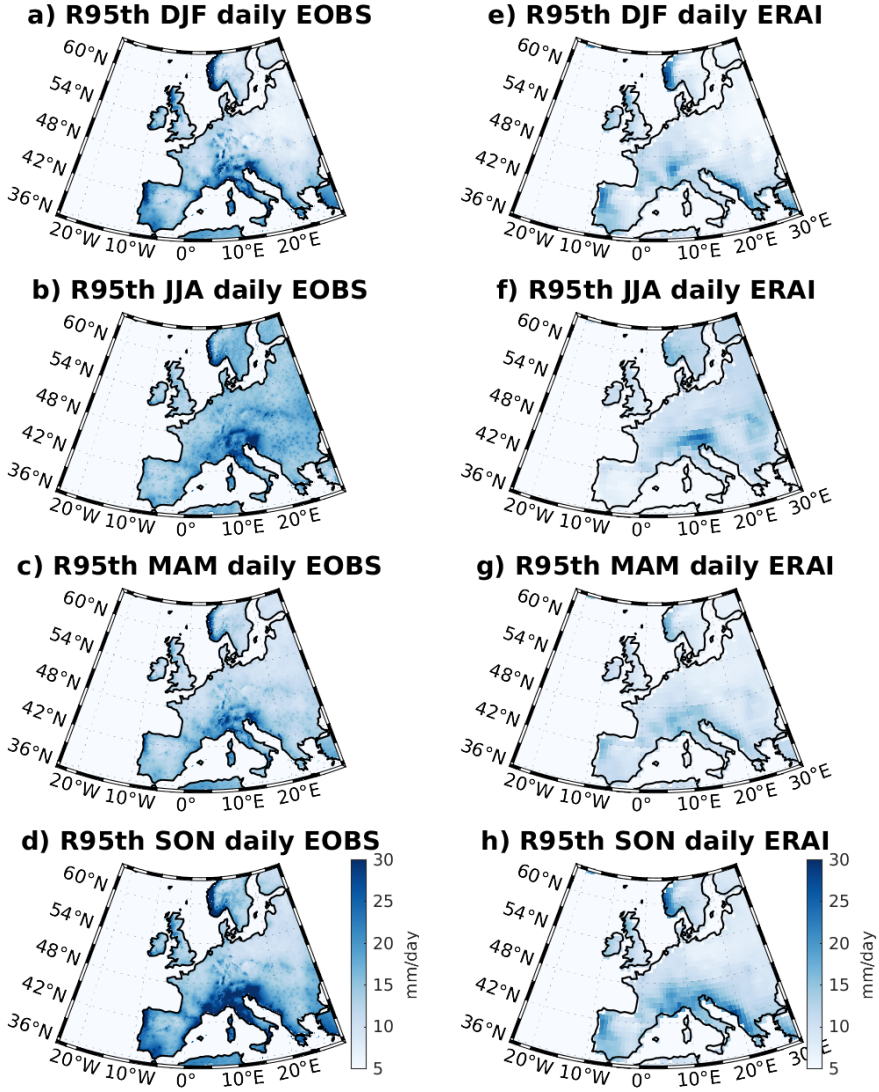

FIGURE 2.2: The value of the 95th percentile of seasonal precipitation using EOBS (left column) and ERA-Interim reanalysis (right column) daily data for the period from 1979 to 2008. (Unit: mm/day)

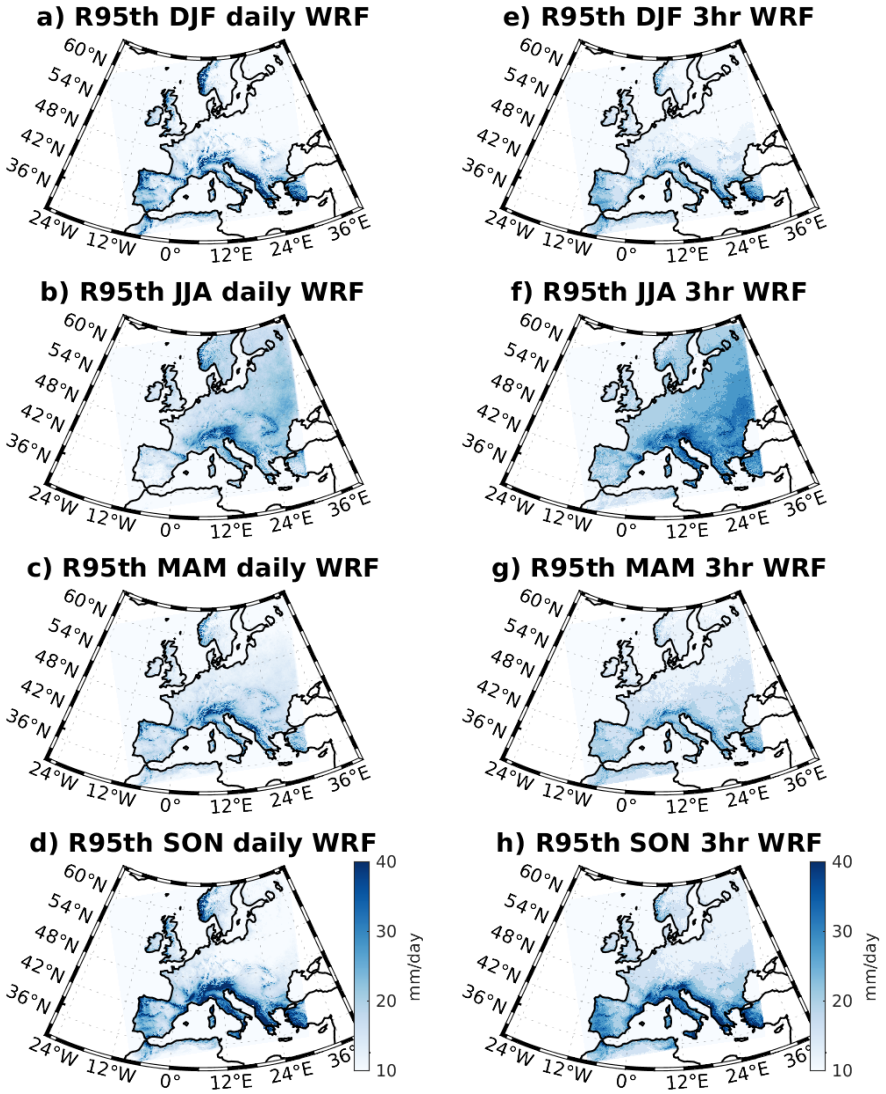

FIGURE 2.3: Similar to figure 2.2, except for WRF daily data (left column), WRF 3-hourly data (right column).

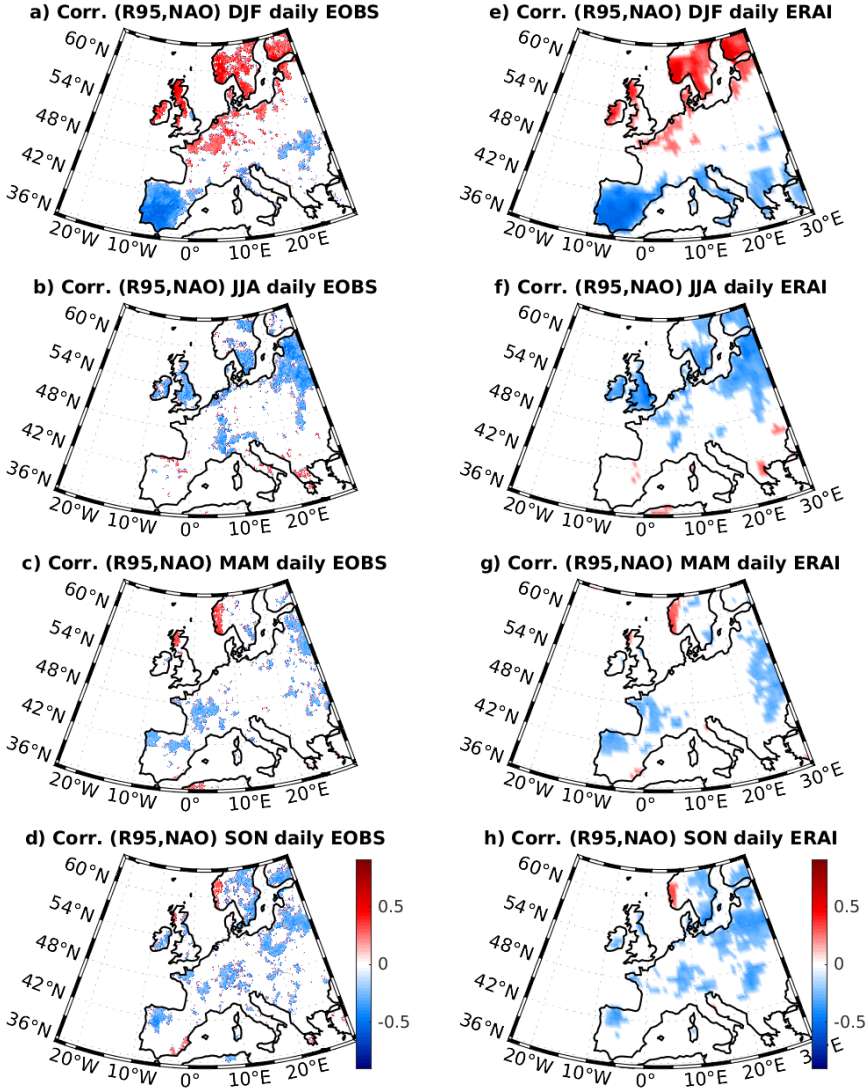

FIGURE 2.4: Temporal correlation coefficient of monthly accumulated precipitation that exceeds the 95th percentile with NAO PC index for: EOBS (left column) and ERA-Interim reanalysis (right column), daily data. Only statistically significant correlation ($p < 0.05$) is shown.

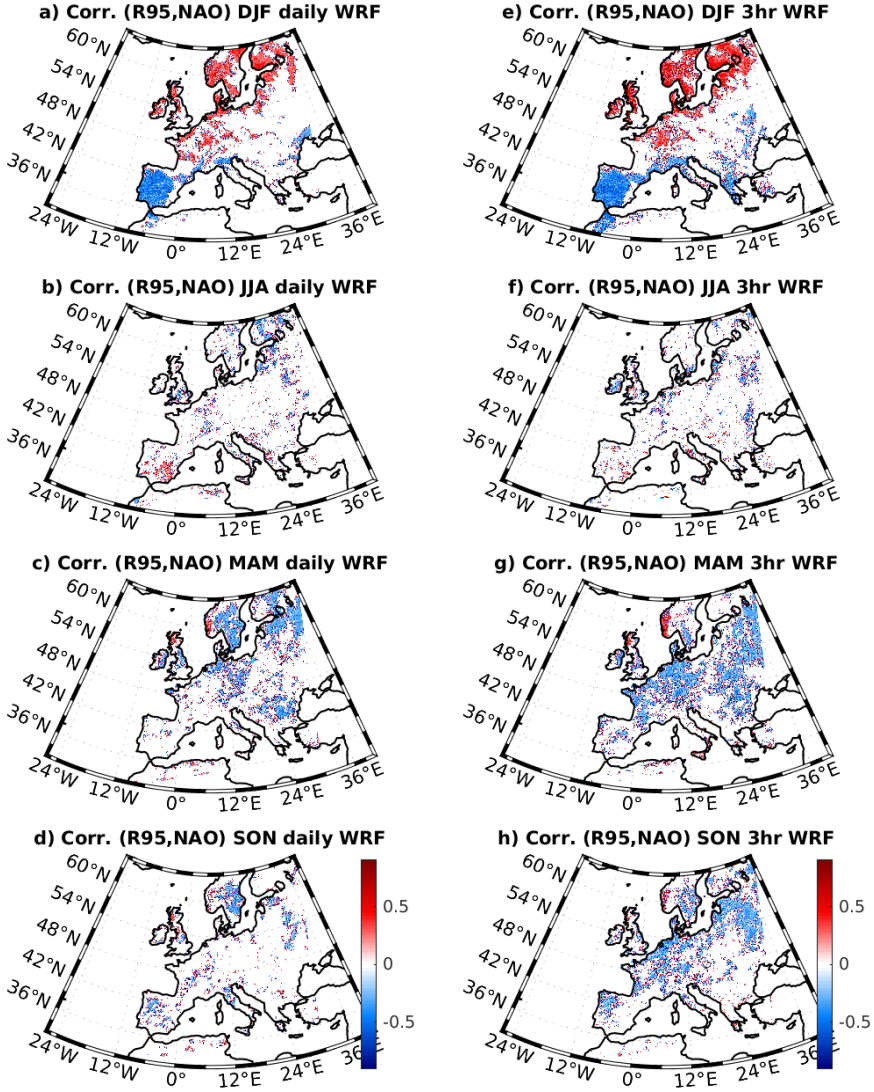

FIGURE 2.5: Similar to figure 2.4, except for WRF daily data (left column), WRF 3-hourly data (right column).

The temporal and spatial high resolutions are also examined using 4 km spatial resolution, daily and 3-hourly temporal resolution. By comparing the 3-hourly WRF simulations in figures (2.4,2.5) for the transition seasons (SON and MAM), negative correlation of the short-lived extreme precipitation events with the NAO become significant for wider regions over Europe. Further positive correlation signal in DJF appears over the Great Alpine Region in WRF 4 km simulation as in figure 2.5(a,e), a signal that is not evident in ERA-Interim reanalysis.

2.3.3 Seasonal Trends of Extreme Precipitation

According to the Clausius-Clapeyron relation, when global temperature increases, the air can hold more moisture. More moisture means more frequent and intense extreme precipitation, as more latent heat released during condensation further increases the buoyancy of the air, favoring further upward motion and thus more condensation. This is concluded by some studies (e.g. Fischer and Knutti (2016), Zolina et al. (2008), and Papalexiou and Montanari (2019)), where rain gauges data and models show that the trend of extreme precipitation is positive in many locations, in correspondence to the warmer climate of the last decades. Here, a similar analysis is followed as in Papalexiou and Montanari (2019), by recording the top 2.5% most extreme precipitation events, then calculating the linear trend of extreme precipitation intensity and frequency of occurrence as detailed in Methods section.

Figures (2.6,2.7) show seasonal trends of extreme precipitation frequency of occurrence for daily EOBS, ERAI and WRF, and WRF 3-hourly time scale. Similarly, figures (2.8,2.9) show seasonal trends of extreme precipitation intensity. Figures (2.11,2.10) show both seasonal trends of frequency and intensity for WRF regridded (to ERA-Interim grid spacing, see Methods section) and ERA5 reanalysis respectively.

For wintertime, panels (a,e) of figures (2.6-2.10) show mostly positive trends over north Europe, and generally negative trends over southern Europe, an aspect that is common for all datasets, except for the 3-hourly timescale, in which positive trends dominate in most of the domain.

The characteristic positive/negative dipole of daily precipitation trends for north/south Europe can be explained by the positive trend of the NAO over the studied period (Scaife et al. (2008), Goodess and Jones (2002), Pinto and Raible (2012), and Santos et al. (2018)), and the general tendency of the NAO to become more positive under global warming conditions (Coppola et al., 2005; Gillett and Fyfe, 2013). Figure 2.13 shows the NAO index for station-based data, highlighting the recent positive trend of the NAO starting from 1965 onward. As the NAO tends to become more positive, extreme precipitation increases in northern Europe, and drier conditions prevail over southern Europe. This wintertime characteristic dipole is summarized in figure 2.14. The figure shows the ratio of the count of the number of grid points with positive trends to the count of the number of grid points with negative trends, divided for Northern and Southern Europe. The separation

latitude is taken at $49^{\circ}N$, which marks the change of the sign of precipitation correlation with winter NAO index in figure 2.4.

Further confirmation to the previously described NAO dependent dipole is carried out. The period of analysis is changed to start from 1990 to 2010 using EOBS dataset. This is motivated by the need to examine a different period with a negative NAO trends. As shown in figure 2.13, the period of 1990-2010 shows a strong negative NAO trend. The trend of extreme precipitation frequency in EOBS is calculated in figure 2.12, and indeed demonstrates the opposite sign of the dipole over Europe (negative (positive) trends in northern (southern) Europe), concluding that winter extreme precipitation events are tied to wintertime NAO variability.

For summer and transition seasons, some agreement in the patterns between EOBS, ERAI, ERA5, and WRF daily are evident (figures 2.6-2.10). However, ERAI and ERA5 fail to capture the correct trend, especially over high orography, emphasizing the important role of resolving convective precipitation using high resolution models (Giorgi et al., 2016).

From this analysis, it seems that ERA-Interim tends to overestimate the large scale precipitation component, even in transition seasons, in which the fraction of precipitation due to convection dominates large scale precipitation. In spring (MAM), figure 2.4g shows that the France and North of the Iberian peninsula are negatively correlated with NAO. These regions have mostly negative extreme precipitation trends (figure 2.6g,2.8g). The reason for this could be the positive trend of spring

NAO over the past decades as in (Santos et al., 2018). Therefore, a negatively correlated spring NAO with a positive trend consequently result in a negative trend of extreme precipitation frequency. On the other hand, despite the negative correlation of spring NAO with extreme precipitation, EOBS and WRF rather show positive trends of extreme precipitation frequency figures (2.6-2.9)c & 2.11(c,g). This can be related to the accountability of the convective precipitation in both EOBS and WRF datasets, while ERA-Interim overestimates large-scale precipitation component.

Moreover, in summer, the Mediterranean sea is considered an important source of moisture feeding extreme precipitation over central Europe (James et al., 2004; Stohl and James, 2005), a source that is driven by the so-called Vb-track, which is characterized by upper level strong south-westerly wind from the Mediterranean driving surface low pressure systems toward central Europe (Bebber, 1891). It has been shown that the Mediterranean is a hot-spot for global warming (Giorgi, 2006) with an increasing SST, especially in the period (2000-2012) (Rayner et al., 2003). (Volosciuk et al., 2016) use atmospheric model simulations to show that a warmer Mediterranean increases precipitation extremes over central Europe. Despite of this, ERA-Interim and ERA5 do not show the pattern of the positive extreme precipitation trends over central Europe and the Alpine region figures (2.6f,2.8f,2.10b,f), while WRF 4 km run succeeds to correct these trends using the dynamical downscaling (figures 2.7b,2.9b) which is consistent with EOBS (figures 2.6b,2.8b).

Most of the individual extreme precipitation time series do not have a significant trend at the 5% significance level. Moreover, signals are

certainly spatially correlated as storms and large scale environmental conditions generate spatial precipitation patterns. Accounting for these caveats, one can establish over the study region whether the signals are consistent with a null hypothesis of stationarity in the occurrence and intensity of extreme precipitation or not. To this end, it is useful to compute the ratio of the count of positive to the count of negative trends over the domains as shown in figures (2.6-2.11) for extreme precipitation frequency and intensity (figure 2.15). A ratio higher than 1 means that positive trend in the frequency of occurrence is more dominant than negative trends. The opposite applies for ratios less than 1. As the number of degrees of freedom to compute it increases, the ratio should approach one in the null hypothesis of stationarity. The EOBS dataset indicates a ratio smaller than one for DJF and larger than one for all other seasons. Wintertime extreme precipitation, as it has already been discussed, mainly reflect a dynamical change in the large scale atmospheric circulation associated to the NAO phase. The fact that the locations in which extremes decrease are more than the locations in which they increase can be linked to the fact that a large region in Europe has precipitation which are anti-correlated with NAO. Extreme precipitation in the rest of the year show an overall increasing trend both in the frequency of occurrence and in their intensity (ratio larger than one) in the EOBS dataset, suggesting that the overall increase expected in response to a warming world could be responsible for the observed signal over Europe.

Figure 2.15 shows that ERA-Interim and ERA5 fail to capture the increasing frequency and intensity of extreme precipitation in summer

and transition seasons, while they succeed in representing extreme precipitation changes in winter. This latter result is consistent with its link to NAO variability, that is well represented in reanalysis products. An improvement in using ERA5 with respect to ERA-Interim is evident in SON for frequency trends, in MAM and SON for intensity trends. This could be due to the improved convective precipitation parameterization in ERA5 (Hersbach et al., 2020).

Higher temporal and spatial resolutions from WRF dynamical downscaling simulations show more consistent ratios with respect to gridded observation data (EOBS), for which the ratio of the number of positive to negative trends for non-winter seasons is captured. During fall, however, high resolution WRF output indicates a larger increase of intense precipitation over time than the gridded product EOBS.

For the short-duration extreme precipitation events (WRF 3-hourly), figures (2.7,2.9 right column) & 2.15 show that, regardless of the season, positive trends of extreme precipitation frequency and intensity dominate the European domain, which is consistent with (Hosseinzadehtalaei, Tabari, and Willems, 2020; Cannon and Innocenti, 2019; Kendon et al., 2014). Moreover, figure 2.9(e-h) also shows the previously mentioned general positive trend. However, it also illustrates that the summer (JJA) has the strongest and most widespread positive trends with respect to other seasons. This is discussed by (Mishra, Wallace, and Lettenmaier, 2012; Lenderink and Meijgaard, 2010), where it was shown that in summer the dependence of short-duration extreme precipitation on air temperature (Clausius-Clapeyron scaling) doubles with respect to winter.

To further investigate the added value of the high resolution and the dynamical downscaling that resolves convection, the analysis is repeated on WRF simulations after statistically regridding (upscaling) the data (see Methods) to a resolution equivalent to that of ERA-Interim. Figure 2.11 shows seasonal trends of extreme precipitation frequency and intensity for the regridded WRF simulations. The figure shows that the trends of regridded WRF simulations in DJF do not change, and are consistent with those in EOBS and ERA-Interim. In summer and transition seasons, regridded WRF still shows trends similar to these of the high resolution simulations. This is also shown in figure 2.15, where upscaling WRF from 4 km to a lower resolution does not dissipate the added value of the high resolution, showing the same ratio as the high resolution data in all season.

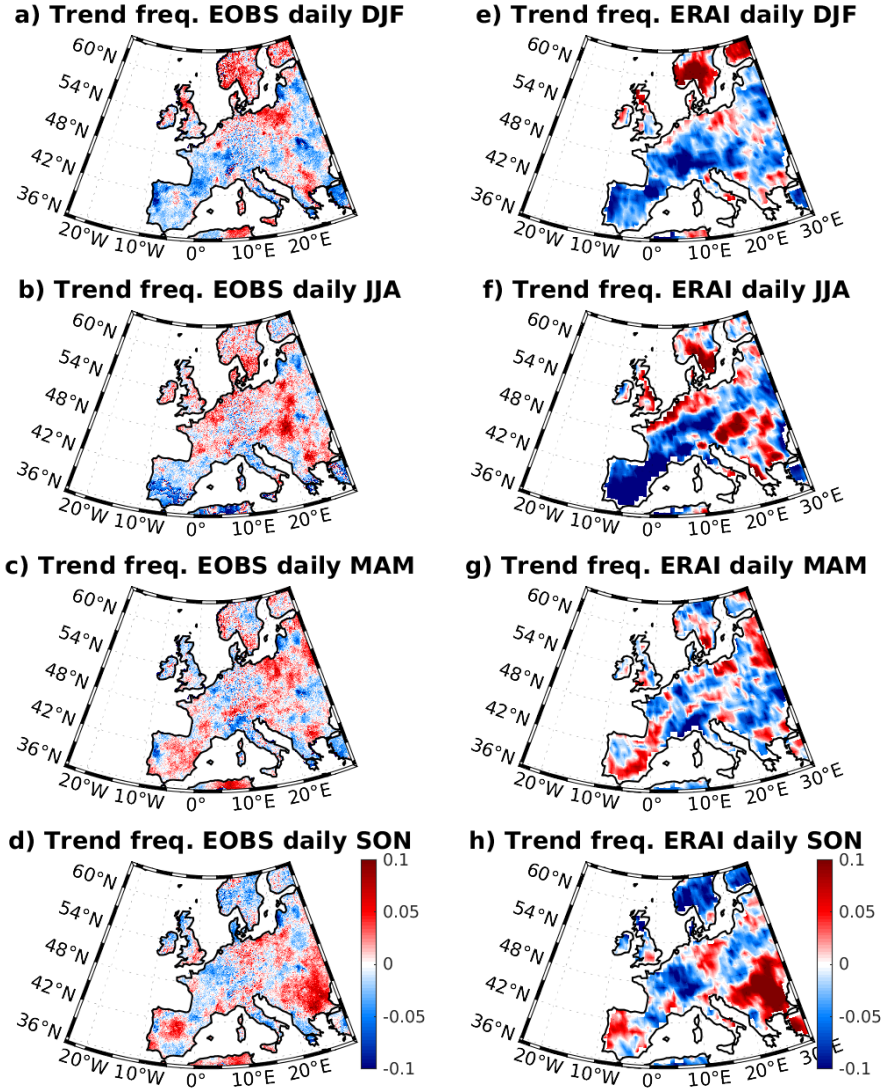

FIGURE 2.6: Seasonal trends of extreme precipitation events frequency for the daily data of EOBS (left column) and ERA-Interim reanalysis (right column). Unit: (1/year).

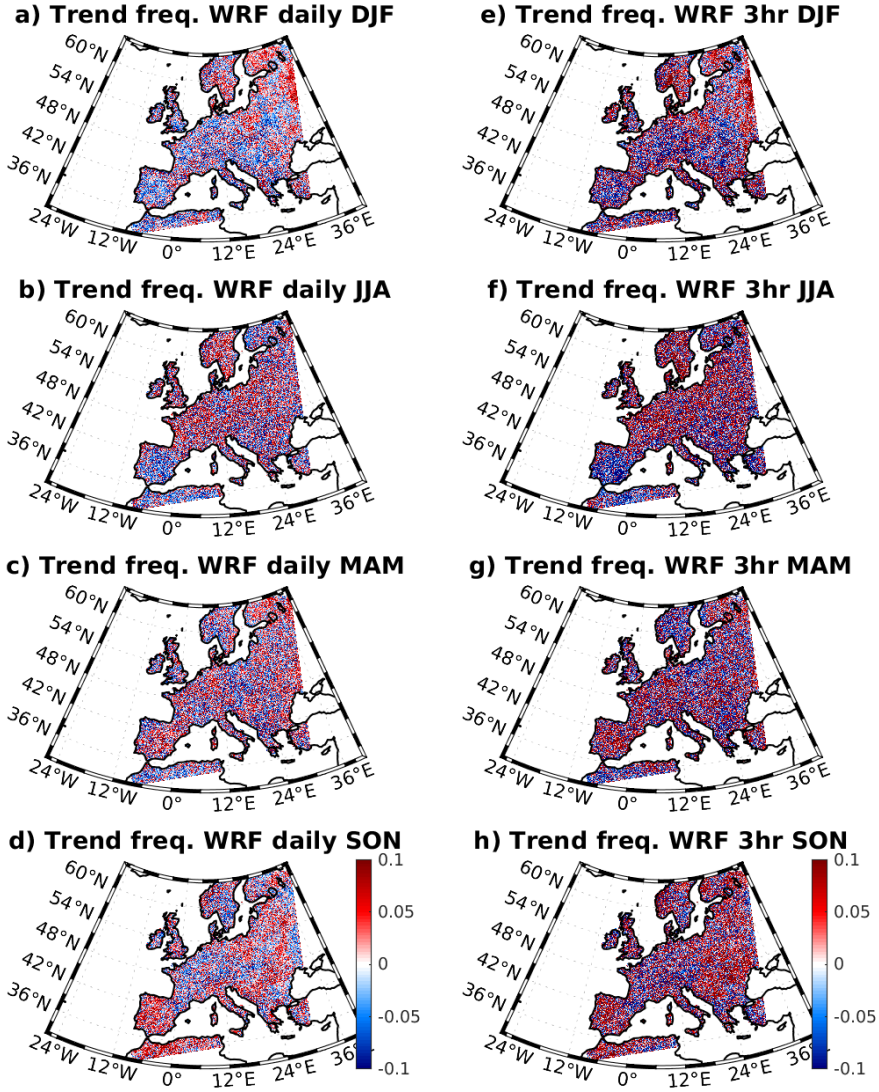

FIGURE 2.7: Similar to figure 2.6, except for WRF daily data (left column), WRF 3-hourly data (right column).

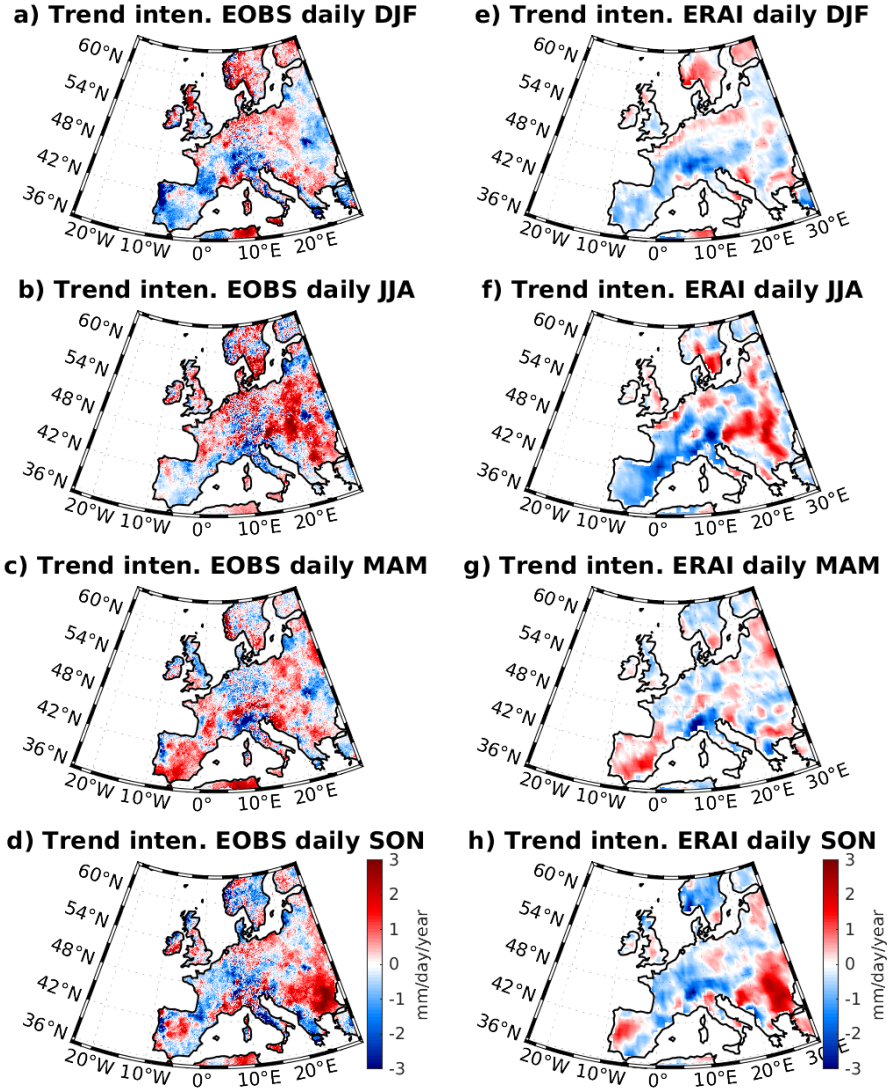

FIGURE 2.8: Seasonal trends of extreme precipitation intensity for the daily data of EOBS (left column) and ERA-Interim reanalysis (right column). Unit: (mm/day/year).

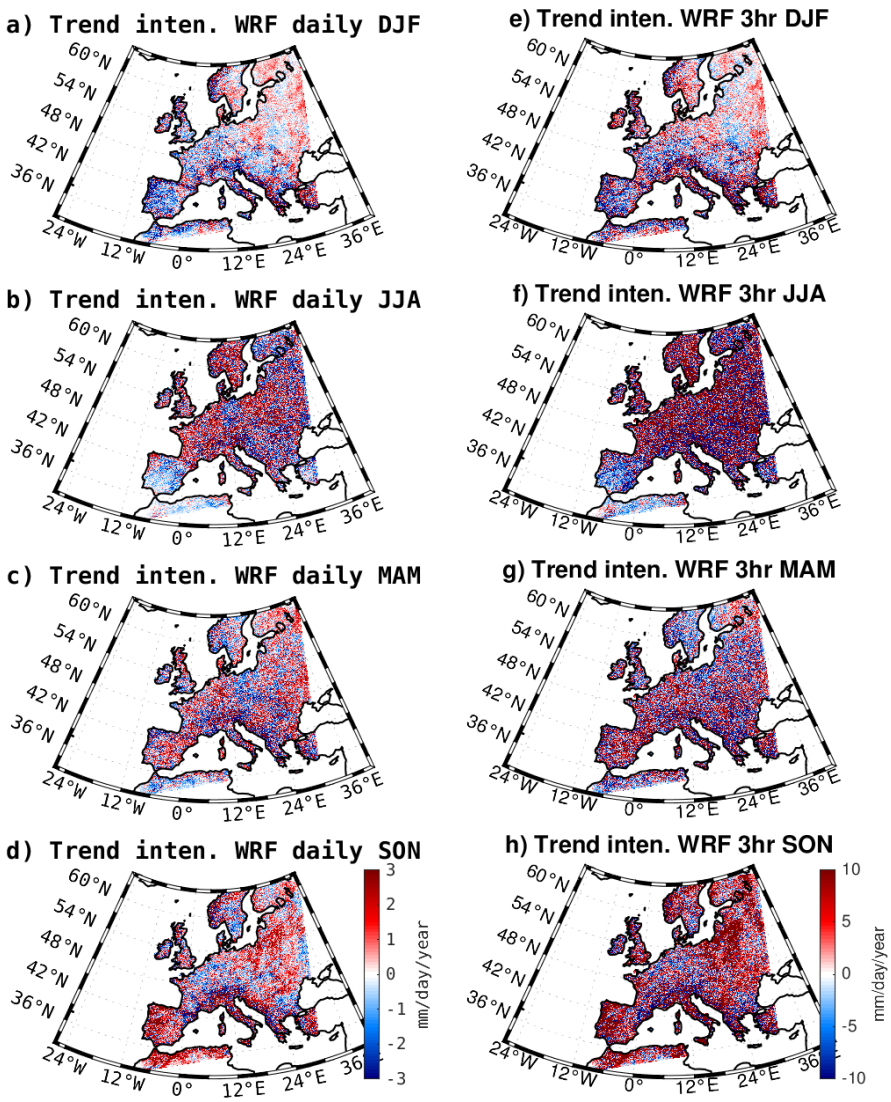

FIGURE 2.9: Similar to figure 2.8, except for WRF daily data (left column), WRF 3-hourly data (right column).

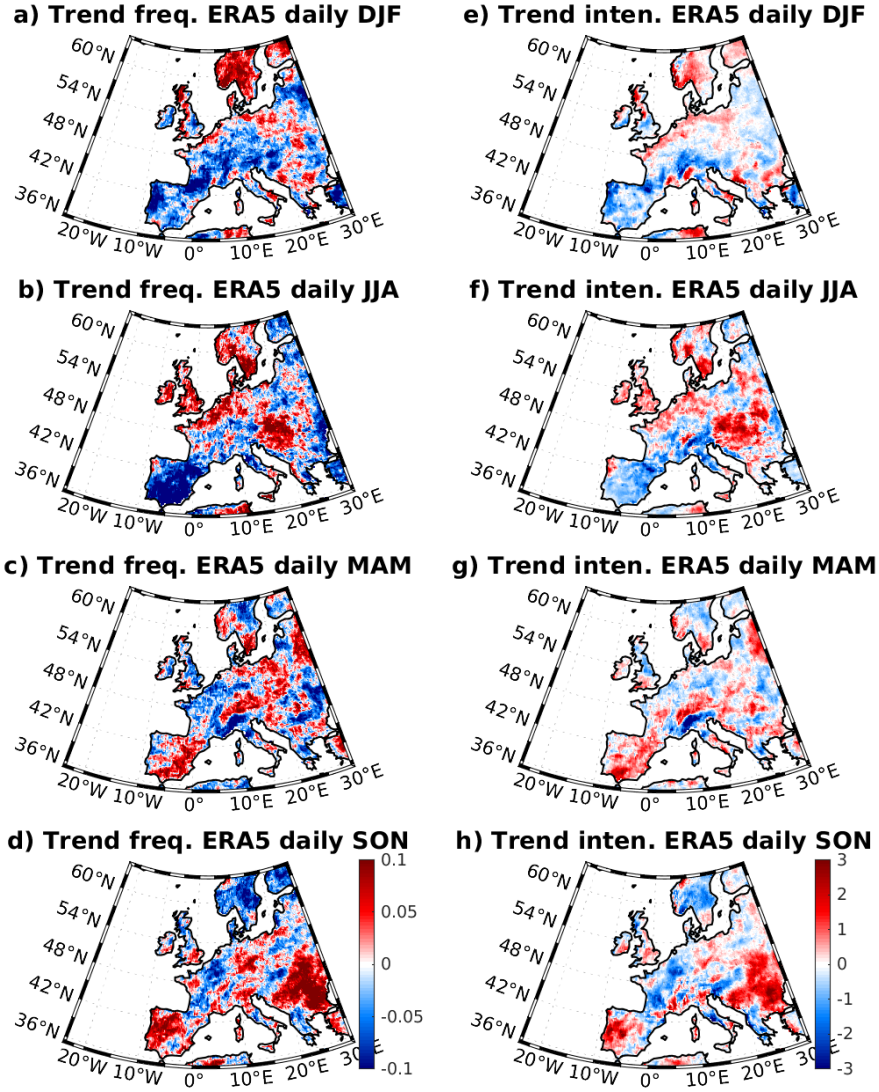

FIGURE 2.10: Seasonal trends of extreme precipitation for ERA5 daily data. Left column: Frequency trends (1/year). Right column: Intensity trends (mm/day/year).

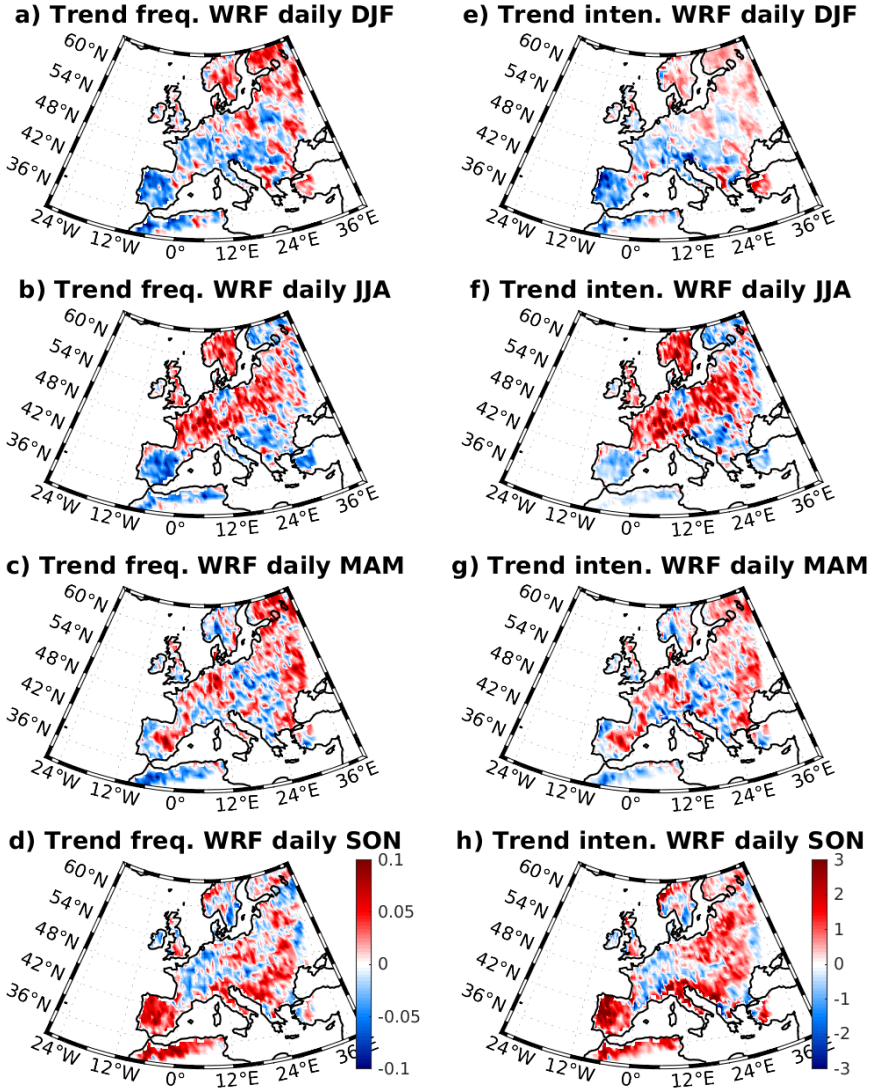

FIGURE 2.11: Seasonal trends of extreme precipitation for WRF regridded daily data. Left column: Frequency trends (1/year). Right column: Intensity trends (mm/day/year).

It is concluded that the difference with respect to the ERA reanalysis is not related to the size of the grid box over which averages are taken, but indeed it is related to differences in the small scale dynamics. Therefore, it is hypothesized that this is due to the convective parameterization used in the reanalysis, that provides different results from the mesoscale convection resolving WRF downscaling. It is concluded that the dynamical downscaling at high resolution has a relevant impact on the statistics of extreme precipitation.

In closing this chapter, it is worth noting that the NAO mode of variability has been changing over the recent decades under climate change. A positive trend of NAO index is observed in the studied period from 1979-2008 as shown in figure 2.13. Moreover, under a hypothetical scenario of climate warming (IPCC A2 forcing (IPCC, 2000)), in studies such as Coppola et al. (2005) and Gillett and Fyfe (2013) show that the distribution of NAO occurrence continues to change, meaning that the NAO is a variability pattern which depends on the mean climate state. The growth of a new positive NAO regime in the frequency of occurrence of the NAO on the expense of the negative NAO, has consequences on the European climate as shown previously. Therefore, the following chapter further investigates more related dynamics regarding this mode of variability under the light of stratosphere-troposphere coupling.

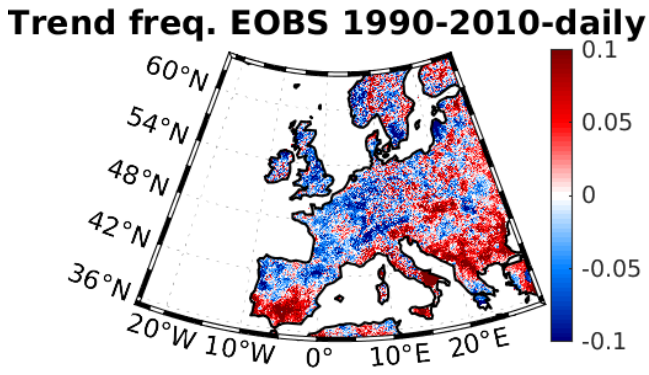

FIGURE 2.12: Winter trend of extreme precipitation for EOBS daily data for the period 1990-2010 which coincides with a negative trend of NAO index. Unit: 1/year.

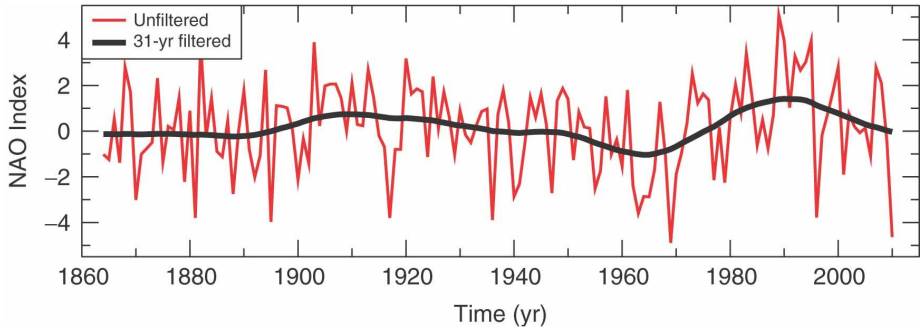

FIGURE 2.13: Time series of the station-based NAO index from 1864 to 2009 for the season DJFM. Unfiltered data is showing year to year (Red); a 31-year filter is applied illustrating the low-frequency variability (Black). (From Pinto and Raible (2012))

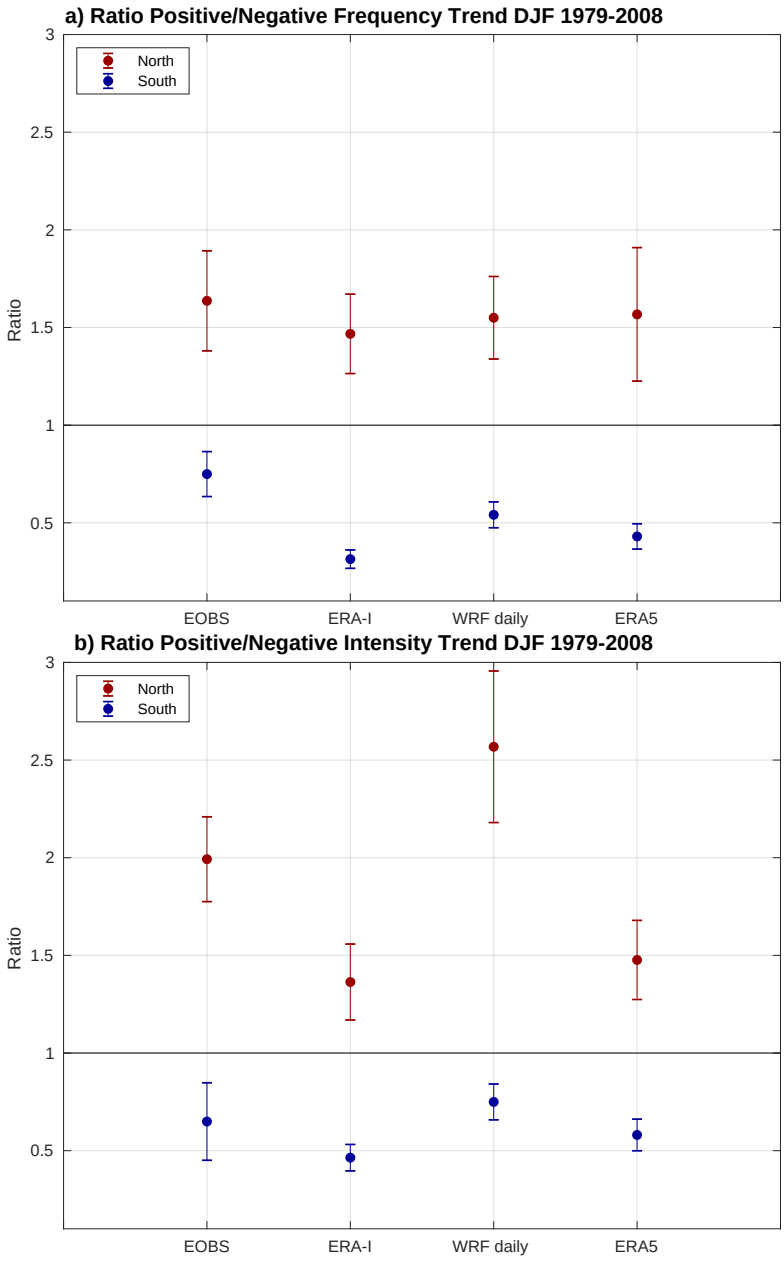

FIGURE 2.14: Wintertime (DJF) ratio of positive to negative trends of extreme precipitation events frequency in EOBS, ERA-Interim and ERA5 reanalysis, WRF daily data. Trend summation is calculated for northern and southern Europe. North: $49.1°N - 63°N$. South: $34°N - 49°N$. Error bars indicate the spread of the ratio by random sub-sampling within the domain.

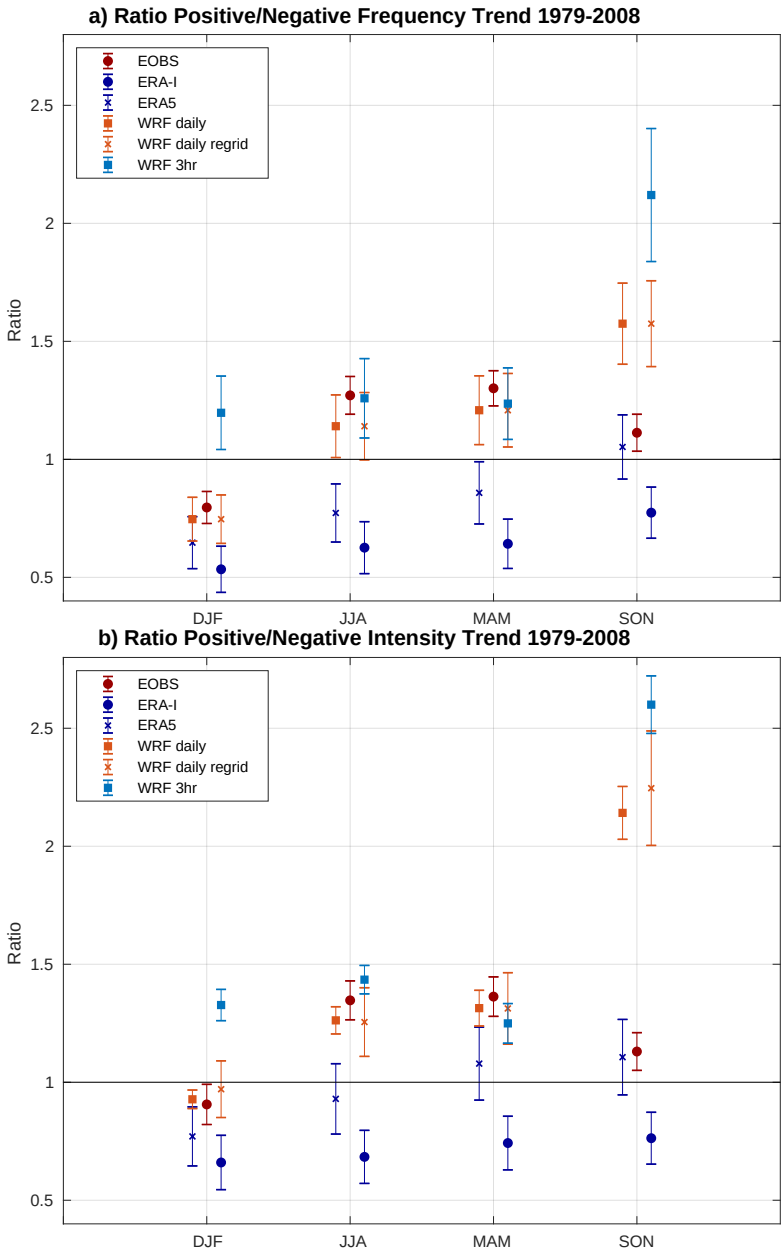

FIGURE 2.15: Ratio of positive to negative trends of extreme precipitation events frequency in EOBS, ERA-Interim reanalysis, WRF daily data at 4 km and regridded to ERA grid (WRF daily regrid), and WRF 3-hourly data, as shown in figures (2.6,2.7). Error bars indicate the spread of the ratio by random sub-sampling within the domain.

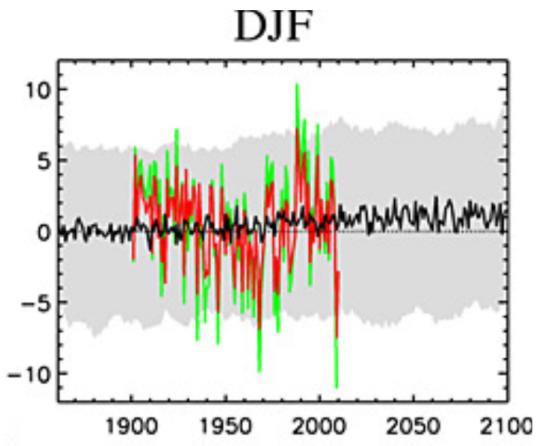

FIGURE 2.16: NAO index for the mean of 37 CMIP5 models merged historical and RCP 4.5 simulations (black) for DJF. The gray band shows the range from the second to the 36th largest anomaly in each year based on a single ensemble member from each of the 37 models, a non-parametric estimate of the 5–95% confidence range. Colored lines show observational annular mode indices derived from HadSLP2r (red) and 20CR (green) data. Simulated anomalies are shown relative to an 1861–1900 climatology, and observations are centered on the multi-model ensemble mean over the period for which they are shown. From Gillett and Fyfe (2013)

.

Chapter 3

Decoupling of AO and NAO

3.1 Introduction

* The position of the storm track and the seasonal precipitation over Europe and Eastern North America are known to be linked to the phase of the North Atlantic Oscillation (NAO) which is the most prominent pattern of atmospheric variability over middle and high latitudes in the Northern Hemisphere. The NAO is described as an alternation between two pressure systems, the Azores High and the Icelandic Low, which in turn influences weather conditions over large areas (Walker and Bliss, 1932; Hurrell, 1995). The Arctic Oscillation (AO, also known as the Northern Annular Mode, NAM) has been introduced (Thompson and Wallace, 1998; Thompson and Wallace, 2000; Thompson, Wallace, and Hegerl, 2000) as a hemispheric climate variability pattern characterized by a primary center of action over the Arctic, and two opposite centers of action in mid-latitudes, one over the North Pacific, and

*The contents of this chapter are mostly published in the article: **Hamouda M.E., Pasquero C, Tziperman E.. Decoupling of the Arctic Oscillation and North Atlantic Oscillation in a warmer climate, Nature Climate Change. DOI:** 10.1038/s41558 − 020 − 00966 − 8**. *Online January 11, 2021***

the other over the North Atlantic. A negative AO is usually associated with pronounced meridional wind patterns and has been linked with the occurrence of surface extremes in the mid latitudes (Cohen et al., 2014). Despite the annular (zonally-symmetric) structure that characterizes the AO, sea level pressure (SLP) anomalies in the North Atlantic and North Pacific centers of action are not correlated (Ambaum, Hoskins, and Stephenson, 2001), suggesting that each one of them can exist independently of the other.

The present-day monthly temporal correlation between AO and NAO is very high, with correlation coefficients up to 0.95 (Wanner et al., 2001; Deser, 2000). For this reason, the NAO is often referred to as the local manifestation of the AO, and the two terms have been used interchangeably (e.g., (Cohen et al., 2014; Holland, 2003; Baldwin and Dunkerton, 2001; Cohen and Barlow, 2005)). Their variability has been shown to be affected by stratospheric anomalies: in winter, the correlation between the 90-days low pass filtered anomalies of 10 hPa and 1000 hPa geopotential height exceeds 0.65, when surface anomaly time series is lagged by about three weeks, meaning that stratospheric anomalies are good precursors to surface NAO/AO conditions (Baldwin and Dunkerton, 2001; Baldwin and Dunkerton, 1999). On the other hand, the stratospheric polar vortex is known to be influenced by various tropospheric phenomena, such as tropical and extra-tropical variability, including El Niño Southern Oscillation (ENSO) (Butler and Polvani, 2011), Quasi-Biennial Oscillation (QBO) (Baldwin et al., 2001), the Madden-Julian tropical atmospheric oscillation (Jiang, Feldstein, and Lee, 2017; Garfinkel et al., 2012; Kang and Tziperman, 2017) and sea-ice or snow

cover changes in the Arctic region (Wu and Zhang, 2010; Peings and Magnusdottir, 2014; García-Serrano et al., 2015; Ruggieri et al., 2017; Kretschmer et al., 2016; Nakamura et al., 2016; Cohen et al., 2007). Enhanced air-sea fluxes and/or deep convection generate a delayed warming response in the polar stratosphere, which eventually often triggers a negative NAO/AO phase (Jiang, Feldstein, and Lee, 2017; García-Serrano et al., 2015; Kretschmer et al., 2016; Deser, Tomas, and Peng, 2007).

In this study, the dependence of AO and NAO on climate mean state is investigated, showing that their correlation breaks down in a warmer climate, and suggesting a sufficient condition for the change. Then, a discussion of the implications of these modifications on the stratosphere-troposphere coupling follows. For this purpose, the results obtained from the Coupled Model Intercomparison Project Phase 5 (CMIP5) for the historical period and for the Representative Concentration Pathway 8.5 (RCP8.5) scenario, and from simulations of an intermediate complexity model are used, and compared with reanalysis data. The present-day climate with the most extreme climatic scenario of the representative concentration pathway, RCP8.5, during the 23rd century are compared. This time frame is chosen to shed light on the theoretical behavior of these coupled modes of variability and demonstrate that they can behave very differently under large climate forcing.

3.2 Data and Methods

3.2.1 Data

The adopted reanalysis presented in the study is obtained from the NCEP Climate Forecast System Reanalysis (CFSR) (Saha et al., 2010), for SLP and geopotential height from 1000 to 10 hPa levels in the period from 1979 to 2018. The spatial resolution is $0.5° \times 0.5°$. The reanalysis from the European Centre for Medium-Range Weather Forecasts (ECMWF) ERA-Interim for SLP is also demonstrated, in the period from 1979 to 2018. The spatial resolution is 80 km (T255 spectral).

Model data was obtained from the Coupled Models Intercomparison Project 5 (CMIP5). The following CMIP5 models were used: MPI-ESM-LR (Raddatz et al., 2007), IPSL-CM5A-LR (Dufresne, Foujols, and Denvil, 2013), CCSM4 (Gent et al., 2011), CNRM-CM5 (Voldoire, Sanchez-Gomez, and Mélia, 2013), HadGEM2-ES (Johns et al., 2006), and GISS-E2-R (Schmidt et al., 2014). They comprise all models available for 23rd Century in the RCP8.5 scenario. No a-priori model selection has been performed. All models were re-gridded to a common $2.5° \times 2.5°$ resolution. The historical period (Hist) includes the data from 1901 to 2000, and the considered period for (RCP8.5) projections, is from 2201 to 2300.

3.2.2 Definition of AO, NAO

The Arctic oscillation is defined as in Thompson and Wallace (1998) as the leading mode of the Empirical Orthogonal Function (EOF) analysis (see section 3.2.3) for SLP anomalies for the hemisphere north of

$20°N$. Similarly, the North Atlantic Oscillation is defined as in Hurrell and Deser (2009) by calculating the leading mode of the Empirical Orthogonal Function (EOF) for SLP anomalies, for the domain $(90°W - 40°E, 20°N - 80°N)$.

Monthly data of December, January, and February (DJF) is considered, after removal of the climatological seasonal cycle. The data is detrended and is weighted by the square root of cosine of latitude(North et al., 1982) before computing the covariance matrix.

For the temporal correlation in figure 3.3b, to take into account the non-stationarity of the correlation within the 100 years of historical and RCP8.5, the spread is obtained by randomly sub-sampling model runs to 40 years (which is equivalent to the length of reanalysis), then calculating mean correlation coefficient (point) and the standard deviation (error bar), as presented in figure 3.3b.

The spatial correlation in figure 3.3(a,c) is calculated by regridding reanalysis and models to a common 2.5° × 2.5° grid. In case of AO/NAO correlations, SLP anomalies north of 20°N are regressed onto the NAO index, and the obtained pattern is correlated to AO pattern.

3.2.3 Empirical Orthogonal Function Analysis

Using Eigenvectors

Based on Peixoto and Oort (1992). Consider N vectors of the size $M \times 1$, $\mathbf{f}_n = f_{mn}$, to be detrended sea level pressure anomalies, weighted by $\sqrt{\cos(lat)}$. Each vector represents data at a given time. The covariance matrix C is defined as:

$$C_{M\times M} = \frac{1}{N} F_{M\times N} F^T_{N\times M} \tag{3.1}$$

whose element $C_{ij} = \frac{1}{N}\sum_{n=1}^{N} f_{in} f_{jn}$ so that each entry in the $M \times M$ matrix C contains the temporal covariance between two corresponding spatial points.

Eigenvectors of C satisfy:

$$C\mathbf{u}_j = \lambda \mathbf{u}_j \tag{3.2}$$

The constrained optimization problem of maximization and requiring $\mathbf{u}_j$ to be of unit magnitude is solved using Lagrange multipliers by maximizing:

$$\mathbf{u}_j^T C \mathbf{u}_j + \lambda(1 - \mathbf{u}_j^T \mathbf{u}_j) \tag{3.3}$$

Because the covariance matrix is symmetric, the eigenvectors $\mathbf{u}_j$ are orthogonal. The eigenvector $\mathbf{u}_j$ is maximized, and is equal to the corresponding eigenvalue:

$$\mathbf{u}_j^T C \mathbf{u}_j = \mathbf{u}_j^T \lambda_j \mathbf{u}_j = \lambda_j \tag{3.4}$$

One can project the data at a given time $\mathbf{f}_n$, on a principal component $\mathbf{u}_j$, to obtain thee amplitude for this principal component at that time,

$$t_{jn} = \mathbf{f}_n \cdot \mathbf{u}_j \tag{3.5}$$

The data vector at this time may then be expanded in terms of all of the principal components as:

$$f_n = \sum_{j=1}^{M} \mathbf{u}_j t_{jn} \tag{3.6}$$

Thus, for a given mode j, the amplitude t_{jn} is an $1 \times N$ vector $\mathbf{t}_j$, representing the time series of the amplitude of the principal component $\mathbf{u}_j$. The expansion of the data in terms of the principal components may be written in matrix form as:

$$F_{M\times N} = U_{M\times M} T_{M\times N} \tag{3.7}$$

and multiplying the transpose of the orthogonal matrix of principal components, the time series coefficient is to be given by

$$T = U^T F \tag{3.8}$$

The total variance is the trace of the covariance matrix (sum of diagonal elements), which is also equal to the sum of eigenvalues, $trace(C) = \sum_{j=1}^{M} \lambda_j$. As a result of this, the fraction of the variance explained by the $i$ith PC, $\mathbf{u}_i$ is:

$$\frac{\lambda_i}{\sum_{j=1}^{M} \lambda_j} \tag{3.9}$$

Using Singular Value Decomposition

Based on Banerjee and Roy (2014). Consider N vectors of the size $M \times 1$, $\mathbf{f}_n = f_{mn}$, to be detrended sea level pressure anomalies, weighted by

$\sqrt{\cos(lat)}$. Each vector represents data at a given time. The Singular Value Decomposition (SVD) is:

$$F_{M\times N} = U_{M\times M}\Sigma_{M\times N}V^T_{N\times N} \tag{3.10}$$

The columns of U are eigenvectors of FF^T, and correspond to the eigenvectors of the principal components (EOFs), describing the spatial pattern. The expansion coefficient were obtained from the data by projecting on the EOF vectors using $T = U^T F$. Given the SVD of F, the PC timeseries is obtained by projecting:

$$T = U^T U\Sigma V^T = \Sigma V^T \tag{3.11}$$

The columns of V are the expansion coefficients (PC timeseries).

The advantage of the EOF analysis using SVD is smaller round-off errors, since the data matrix is not squared. However, the advantages of using the covariance matrix is that it is usually ($N > M$), as there are often more time steps than spatial points, and using the covariance matrix then leads to a much smaller problem.

3.2.4 Polar Vortex

For this part of the analysis, the daily data of geopotential height from 1000 hPa to 10 hPa is considered, for the months from November to April. For reanalysis, the period from 1979 to 2018 is used. Due to the limited availability of CMIP5 daily data in the extended RCP8.5 simulations, the analysis is performed using two models: MPI-ESM-LR,

from 1950 to 2000 for the historical period, and from 2281 to 2300 (and 2181-2200, not shown) for the RCP8.5 simulation, and IPSL-CM5A-LR historical simulations from 1901 to 2000, and RCP8.5 simulations from 2201 to 2300. 23rd century daily data from other models are no longer publicly available.

The calculation of the daily Northern Annular Mode (NAM) index in each pressure level is obtained similarly(Baldwin and Dunkerton, 2001) as follows: Geopotential height data are detrended and the climatological seasonal cycle is removed. Then data are weighted by the square root of cosine latitude. For the hemisphere north of 20°N, the first EOF of monthly NDJFMA geopotential height anomalies is calculated, for each pressure level from 1000 hPa to 10 hPa independently. Then daily geopotential height anomalies of NDJFMA are regressed onto the EOF of each level. This results in NAM index (GPH PC index) for each pressure level.

The onset of a weak polar vortex event is defined by the 10 hPa level NAM index. When the 10 hPa index is ≤ -1.5, the composite is captured for all pressure levels from -90 to +90 lag-lead days from the onset which is at 0 days. The same is done for strong polar vortex, except that the NAM index is $\geq +1$.

The NAM is also examined explicitly in the North Atlantic sector, by repeating the same analysis mentioned before, except that for the domain $(90°W - 40°E, 20°N - 80°N)$ as in figure 3.12, 3.13. However, the onset of a weak polar vortex is still using the NAM index of the hemisphere north of 20°N.

Statistical significance of the results shown in fig. 3 and similar, is

done by calculating uncertainty bounds based on random sampling using a boot strapping approach. This is done by randomly sampling the same number of winters from the distribution, and comparing the observed signal to the 95th percentile of the random sampling distribution.

3.2.5 SPEEDY AGCM Simulation

The International Center for Theoretical Physics (ICTP) Atmospheric General Circulation Model (AGCM) is nicknamed SPEEDY for "Simplified Parameterization, primitvE Equation DYnamics", which is based on a spectral dynamical core (Held and Suarez, 1994). It is an intermediate complexity atmospheric model, with eight vertical layers and a triangular truncation of horizontal spectral fields at total wave number 30. It is a hydrostatic, σ-coordinate, spectral transform model in the vorticity-divergence form (Bourke, 1974). The parameterized processes include short- and long-wave radiation, large-scale condensation, convection, surface fluxes of momentum, heat, moisture and vertical diffusion. Convection is represented by a mass-flux scheme that is activated where conditional instability is present and boundary-layer fluxes are obtained by stability-dependent bulk formulae. Further description of the model is in (Molteni, 2003; Kucharski et al., 2013). The representation of the NAO and some applications using the model can be found (Kucharski and Molteni, 2003; Kucharski, Molteni, and Bracco, 2006a). Despite the low-lid stratosphere (30 hPa), the model is able to capture troposphere-stratosphere interactions, such as the triggering of a negative NAO through the stratosphere due to reduced sea ice in Barent

and Kara seas (Ruggieri et al., 2017). Note that for the stratosphere-troposphere coupling, the onset of WPV events is based on NAM index of 30 hPa, considering the EOF that spatially corresponds to the polar vortex and AO in all pressure levels.

Two simulations are conducted, each simulation is 50 years long from 1961 to 2010. A control run (CTL) has monthly prescribed climatological SSTs using Hadley Center (HadSST) data. A perturbation run (Pac_P) is the same as CTL, except that in the North Pacific, a persistent Gaussian-shaped SST warming is added with a peak of 6°C to qualitatively mimic the relative SST conditions in the Pacific and the Atlantic in RCP8.5 (i.e. North Pacific ocean warmer than North Atlantic ocean). figure 3.5 shows the SST forcing used in the experiment.

3.3 Decoupling of the Arctic and North Atlantic Oscillations

Wintertime SLP climatology is characterized by the Aleutian low pressure in the North Pacific, and the (deeper) Icelandic low pressure center in the North Atlantic, with a high pressure center over the polar cap, as in the contours of Fig. 3.1(a,b). The variability of the Atlantic and the Pacific pressure systems are of similar magnitudes in the current climate (shading in Fig. 3.1(a,b)).

The Icelandic and the Aleutian low pressure systems represent the main centers of action of the AO mode of variability (Thompson and Wallace, 1998) as the leading mode of the Empirical Orthogonal Function (EOF) analysis of SLP of the hemisphere north of $20°N$. Similarly, the NAO is defined (Hurrell and Deser, 2009) as the first EOF of SLP in the domain $(90°W - 40°E, 20°N - 80°N)$. The EOF analysis is performed using monthly mean SLP for boreal winter (DJF). It is worth stressing that EOFs are statistical patterns defined to most efficiently characterize the co-variability of the system, but they do not necessarily represent a physical mechanism nor relate to real causal connections among different regions. Notice that with these definitions of AO and NAO, the variability patterns can be different in a different climate, and no link with the patterns identified in the current climate is prescribed.

The observed AO and NAO patterns in the state-of-art reanalysis (NOAA-CFSR) (Saha et al., 2010) are shown in figure 3.1(d,g), based on the period from 1979 to 2018. The historical period is simulated by CMIP5 models from 1901 to 2000. Visual inspection of the variability

patterns computed from the simulation outputs indicates a good agreement between CMIP5 models and reanalysis (see figure 3.1(e,h), and figure 3.2), apart from the model GISS-E2-R, in which the AO pattern has a rather weak center of action over the Atlantic.

A quantification of the performance of CMIP5 models in representing variability patterns in the historical simulations is obtained by computing the spatial correlation between the EOFs derived from the models and from the NOAA-CFSR reanalysis. Results indicate that in all cases, correlation coefficients are larger than 0.87 (figure 3.3a).

The patterns of variability in CMIP5 models were also computed in the RCP8.5 scenario, and results are shown for the period from 2201 to 2300, which represents the warmest global conditions in the simulation. AO variability in a warmer climate weakens significantly over the Atlantic, while it strengthens over the Pacific (compare fig. 3.1(d,e) to fig. 3.1f). Comparison of fig. 3.1(g,h,i) illustrates that no significant change occurs to the NAO pattern.

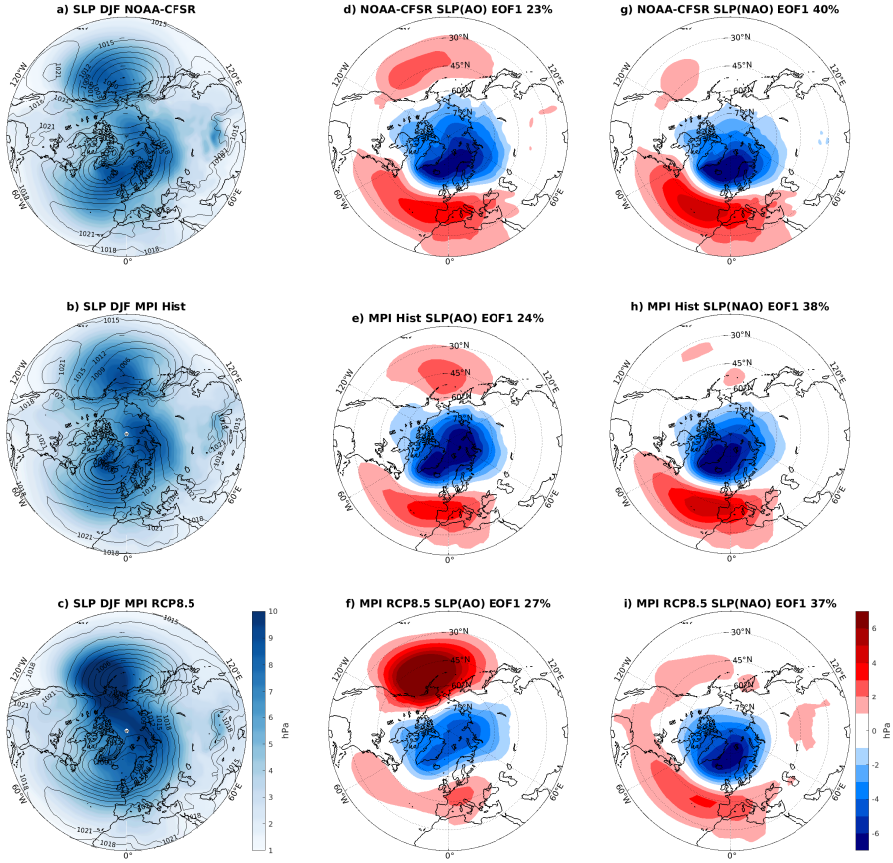

FIGURE 3.1: **Sea level pressure climatology and modes of variability**. Wintertime DJF monthly mean sea level pressure (SLP) (contours in *hPa*), and standard deviation (shading in *hPa*) for a) NOAA-CFSR reanalysis, and MPI-ESM-LR b) historical and c) RCP8.5. The leading EOF mode (AO) for DJF sea level pressure (SLP) for d) NOAA-CFSR reanalysis, and MPI-ESM-LR) historical and f) RCP8.5. (g,h,i) are similar to (d,e,f) except that global SLP is regressed onto the NAO index. The explained variance by the EOF is indicated on top of each panel. Note that the explained variance of (g,h,i) refers only to the variability in the North Atlantic sector. (Shading unit: *hPa*, corresponding to 1 standard deviation of the PC.)

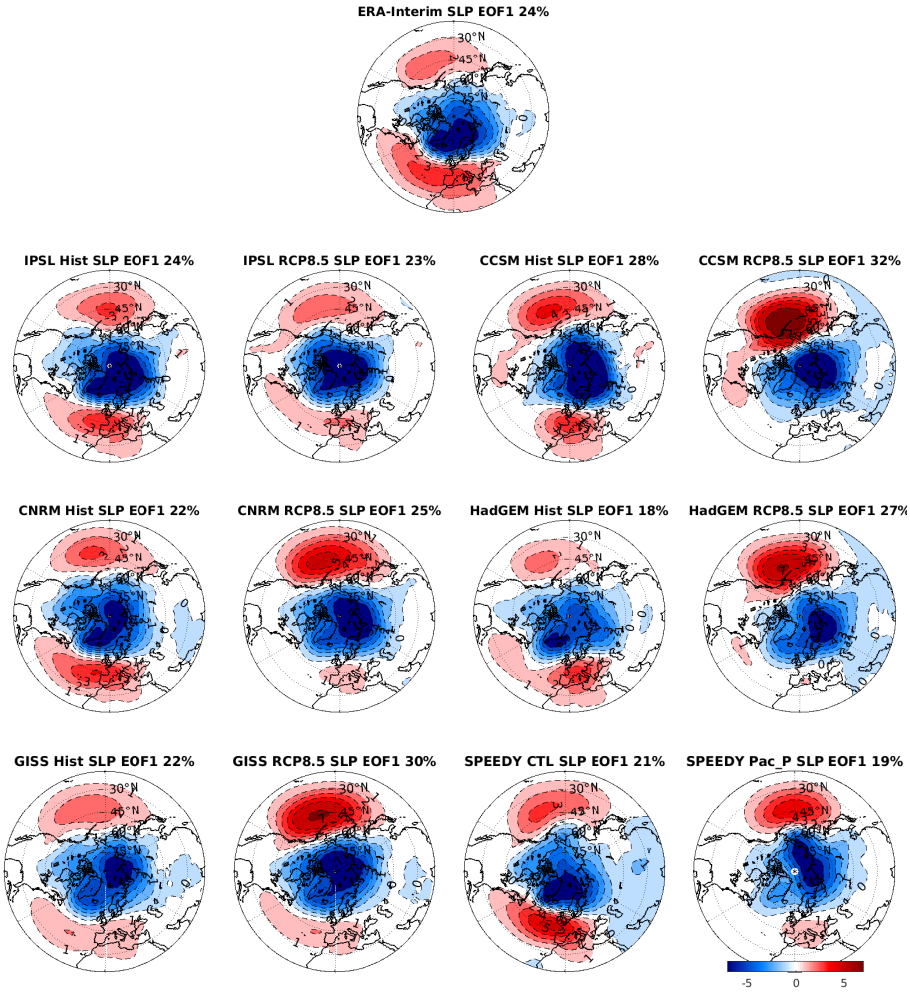

FIGURE 3.2: **The Arctic Oscillation in ERA-Interim reanalysis, historical and RCP8.5.** The leading EOF mode (AO) for wintertime (DJF) sea level pressure (SLP) for Historical (Hist) and RCP8.5 in CMIP5 models. Note that SPEEDY panels refer to the control run using climatology (CTL) and for pacific SST perturbation run (*Pac_P*). (Unit: *hPa* corresponding to 1 standard deviation of the PC). Explained variance by the EOF is indicated on top.

The different response of AO and NAO to a warmer climate is remarkable, considering their strong correlation in the present climate.

In fact, from NOAA-CFSR reanalysis data the spatial correlation coefficient between AO and NAO patterns is 0.93, and the temporal correlation between their principal component (PC) monthly time series is 0.91. Most of the analyzed models show high AO/NAO correlations in the historical period (values higher than 0.81 are found for all the models except for GISS), while in the warmer climate the temporal and spatial correlations mostly decrease (Fig. 3.3(b,c)). The only model that does not show a decrease in the correlations is GISS, which as mentioned before, does not simulate a good AO pattern and has the lowest AO/NAO correlations in the historical period. Therefore it is not considered as a reliable model in this respect. To account for the different size of the samples between reanalysis and model data, error bars in figure 3.3b indicate the standard deviation of the correlation when sub-sampling a 40-year time series within the 100 year period of historical or RCP8.5

The decoupling between AO and NAO is expressed as a weakening or a disappearance of the Atlantic center of action in the AO pattern (see figure 3.2), while the Pacific center of action strengthens. The statistical insight offered by the EOF analysis can be put into perspective by focusing on the following physical mechanism. The alternating change in SLP between middle and high latitudes associated with the AO translates to latitudinal displacement of atmospheric mass, possibly due to planetary wave breaking (Polvani and Saravanan, 2000). A negative AO phase is associated with anomalous high pressure in high latitudes, and a low pressure anomaly in mid latitudes. The implied anomalous mass redistribution is typically expressed in the Atlantic and/or Pacific

basins, not necessarily at the same time (as indicated by the lack of correlation between Pacific and Atlantic anomalies (Deser, 2000)).

The high correlation between NAO and AO in the current climate indicates that the preferred sector for the occurrence of the anomalous meridional eddy fluxes is the North Atlantic, which is warmer than the North Pacific during winter months, and has a more variable jet stream. In the warm climate RCP8.5 scenario, the preferred sector becomes the North Pacific. It is worth noting that this change is associated with a substantially larger increase of sea surface temperature (SST) over the North Pacific compared to the North Atlantic, due to the slowdown of the Atlantic meridional overturning circulation(Chen et al., 2019; Sévellec, Fedorov, and Liu, 2017; Rahmstorf et al., 2015) that results in the so-called Atlantic warming hole (see (Hartman et al., 2013; Alexander et al., 2018), and figure 3.4).

Moreover, in the historical period, the Icelandic low is deeper and as variable as the Aleutian low (Fig. 3.1(a,b) and fig. 3.7a). In the RCP8.5 climate, the variability shifts completely to the Aleutian low, whose winter mean low pressure becomes similar to that of the Icelandic low Fig. (3.1c,3.7a).

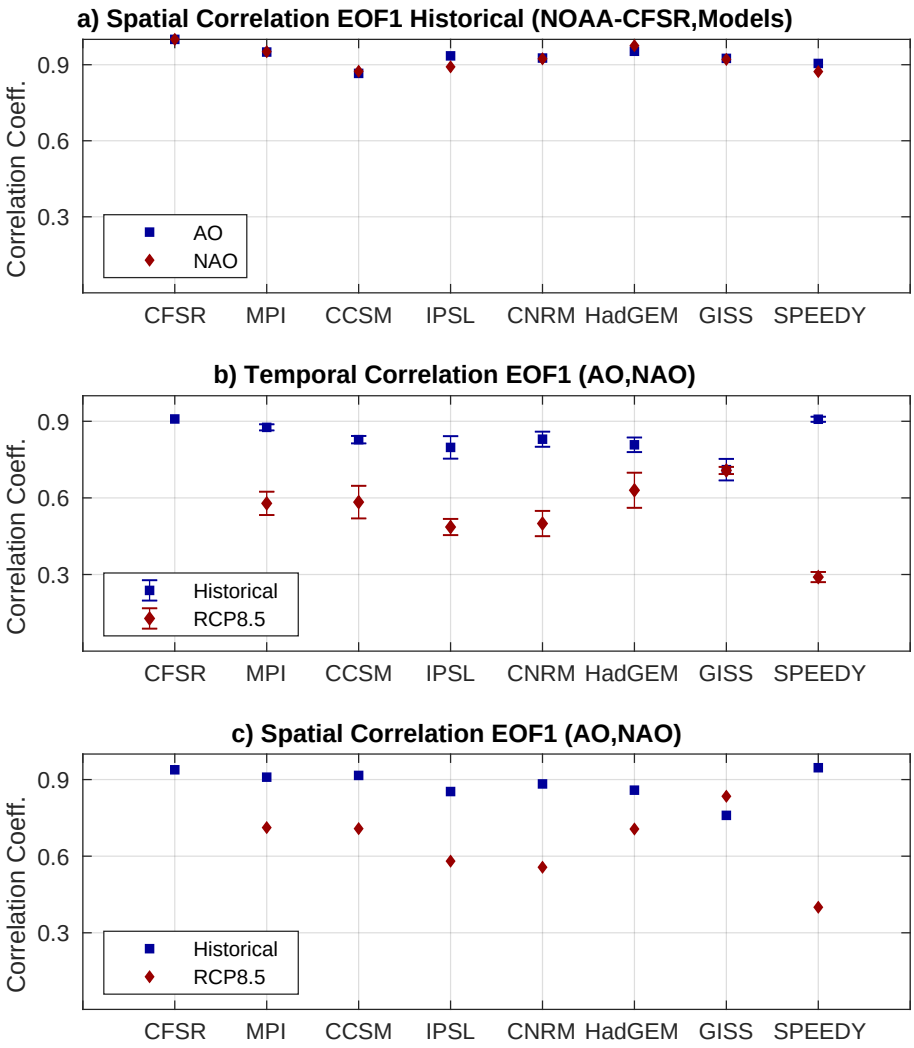

FIGURE 3.3: a) spatial correlation coefficient of the AO & NAO: reanalysis versus models in the historical simulations. b) Temporal correlation of monthly mean sea level pressure SLP (DJF) PC index, AO versus NAO (error bars indicate the standard deviation of the correlation when sub-sampling a 40-year time series within the 100 year period of historical or RCP8.5). c) Spatial correlation of AO versus NAO in the historical and RCP8.5. Sea level pressure (SLP) of the hemisphere north of $20°N$ is regressed onto the NAO PC index and then correlated with AO. Note that SPEEDY red points refer to experiment (Pac_P) where the model is forced by warm SST in the North Pacific. All correlation coefficients are significant with ($p - value < 0.05$).

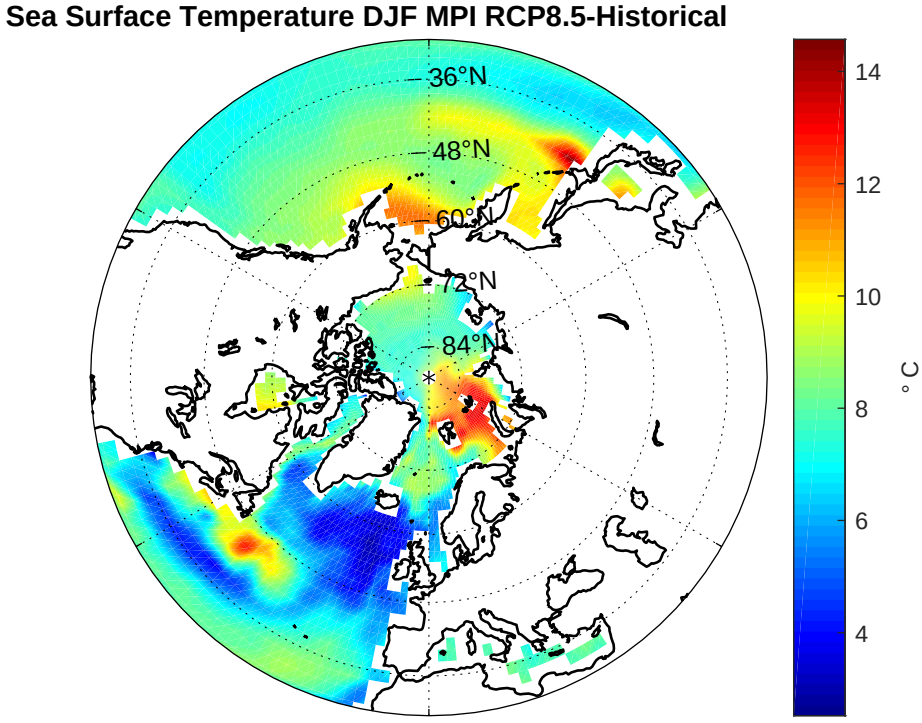

FIGURE 3.4: **Pacific ocean SST response is stronger than the Atlantic**. Climatology response of DJF sea surface temperature (RCP8.5-Historical) from MPI-ESM-LR.

In the 23rd century RCP8.5 scenario simulations, the climate mean state differs in many aspects from the current state. In order to disentangle the responsible climate modification for the observed decoupling, and to propose a possible explanation, a simple experiment is performed using the ICTP Atmospheric General Circulation Model (Molteni, 2003; Kucharski et al., 2013) "SPEEDY AGCM" (further details in Methods). A control simulation (CTL), corresponding to the historical case, is compared with a perturbation run (Pac_P), forcing the model by a 6°C Gaussian-shaped warm SST anomaly in the North

Pacific ocean (experiment setup in figure 3.5a). Such forcing is not totally theoretical, as in late winter of 2014, the north Pacific experienced 2.5°C SST anomalies, known as the Pacific warm blob (Bond et al., 2015). However, the forcing here is amplified to obtain robust signals (further discussion in section 3.8).

The two simulations are identical in their setup, except for SST boundary conditions, which simulate the differential warming of the Atlantic and the Pacific basins. Fig 3.7b shows that the differential warming of SPEEDY modifies the Pacific and the Atlantic low pressure centers: The Aleutian low becomes as deep as the Icelandic low and the SLP variability in the North Pacific sector increases, as in CMIP5 RCP8.5 simulations. Results from this experiment are shown in (Fig. 3.3, Fig. 3.7b and figure 3.2), and and exhibit the same spatial and temporal decoupling of the AO and NAO as observed in RCP8.5 models.

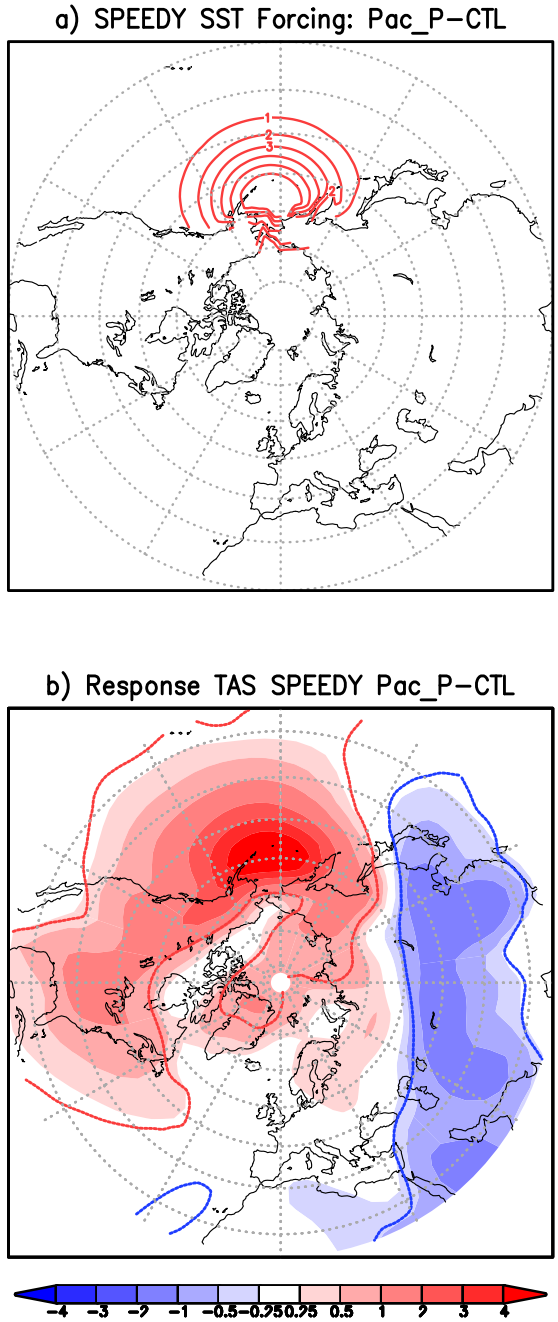

FIGURE 3.5: **SPEEDY General Circulation Model: setup and response.** a) SPEEDY SST forcing design for Pac_P run: Positive Gaussian SST in the North Pacific Ocean with a peak of 6°C. b) Near-surface air temperature response for SPEEDY simulation (Pac_P-CTL), shading unit: °C, contour lines are the 95% statistically significant anomalies using *t-test*.

3.4 The Stratospheric Polar Vortex

In this section, stratosphere-troposphere coupling is examined in light of AO-NAO decoupling. Studies have shown that stratospheric polar vortex anomalies often force AO and NAO variability in the historical (present-day) period, through a downward propagation of the signal in the high latitude troposphere (Baldwin and Dunkerton, 1999; Baldwin and Dunkerton, 2001). Following a similar analysis, the first EOF of November to April monthly mean geopotential height (GPH) anomaly is calculated over the hemisphere north of 20°N at each pressure level independently, and compute the corresponding daily NAM index (GPH PC index) time series by regressing daily GPH anomalies onto the EOF patterns (further details in Methods section). The onset of a weak polar vortex (WPV) event (identified as day 0) is defined when the non-dimensional NAM index at 10 hPa is less then or equal to -1.5.

Fig. 3.6 shows a composite of the time-height development of the NAM index three months prior and after the onset of WPV events, for a) NOAA-CFSR reanalysis, and the MPI-ESM-LR model for b) historical, c) RCP8.5 simulations. Composites of strong polar vortex are shown in figure 3.8. In addition, corresponding analysis of events in the IPSL model in figure 3.9, and for SPEEDY in figure 3.11).

Reanalysis and model historical results both show that, on average, in the present climate, the WPV signal propagates downward from the stratosphere triggering a negative AO phase on the surface within 2–4 weeks (consistent with Baldwin and Dunkerton (2001)). This top-down forcing generates high pressure anomalies over the Arctic and the

associated low pressure anomalies over the Pacific and Atlantic mid-latitudes. Both AO and NAO are triggered by the same stratospheric conditions.

Remarkably, in RCP8.5, surface signals precede the onset of a WPV event. It has already been shown that surface conditions, such as sea ice or snow cover anomalies, can excite Rossby waves that propagate into the stratosphere affecting the polar vortex (Peings and Magnusdottir, 2014; García-Serrano et al., 2015; Ruggieri et al., 2017; Nakamura et al., 2016; Cohen et al., 2007). Here, surface anomalies preceding the onset of WPV events in MPI RCP8.5 scenario and SPEEDY Pac_P experiment are shown in Fig. 3.7(c,d) (also figure 3.10, where the same plot is reproduced for IPSL model) as the composite of geopotential height anomalies for the average of 15 to 10 days prior to a WPV event: A strong low pressure over the Pacific and a high pressure over Eurasia lead the stratospheric anomaly. This pattern projects onto the negative AO conditions in the Pacific sector (strong anomalies of opposite signs over the Arctic and over the mid-latitudes in the Pacific, where SLP has a pronounced negative anomaly).

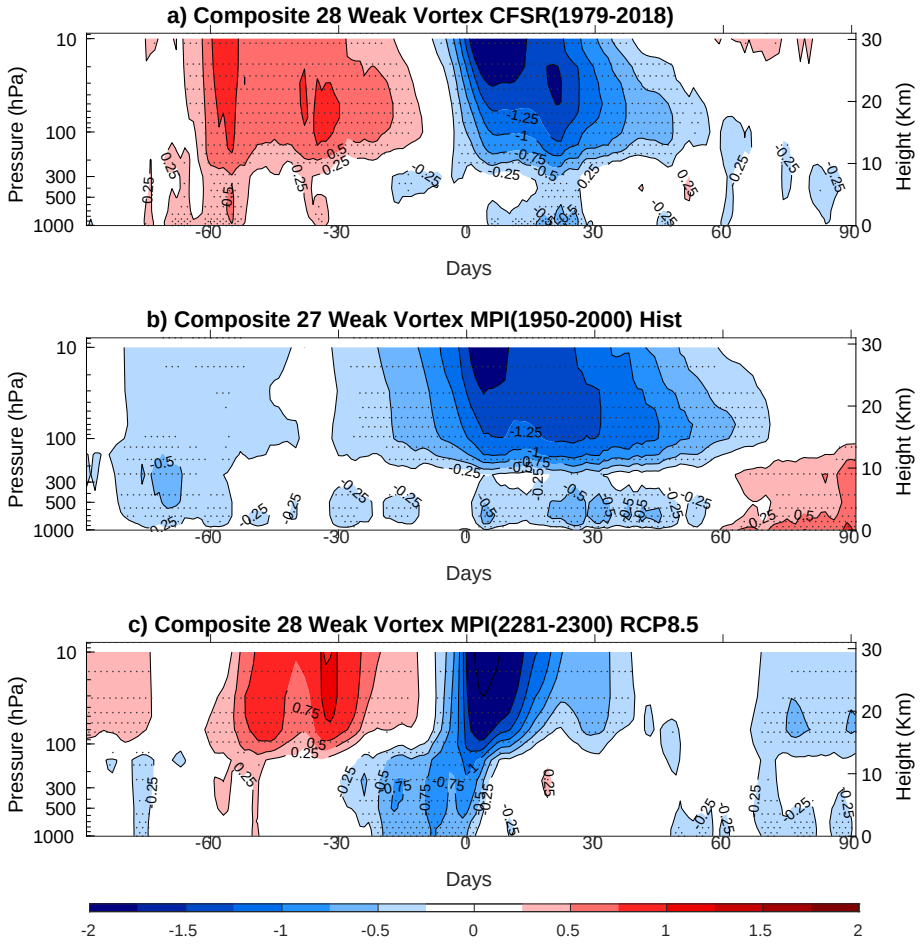

FIGURE 3.6: **Stratosphere-Troposphere coupling: Weak Polar Vortex.** Composite of time-height development of weak polar vortex (WPV) events using NAM index (dimensionless) for a) NOAA-CFSR reanalysis, b) MPI Historical, c) MPI RCP8.5. The condition for a WPV event is when the 10 hPa NAM index is ≤ -1.5. Stippling shows the 95% statistically significant anomalies using bootstrapping approach.

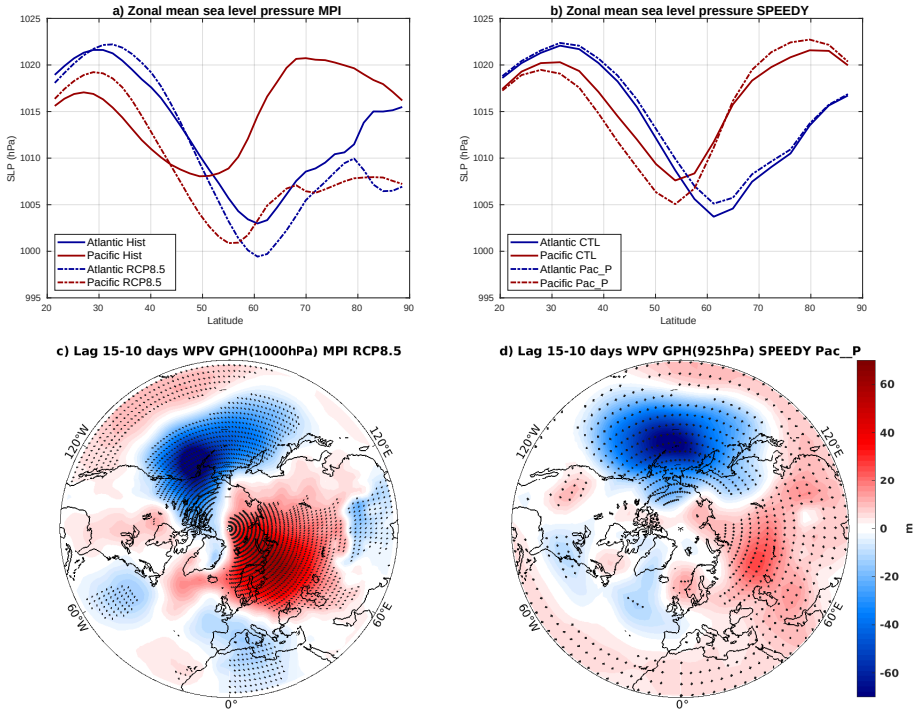

FIGURE 3.7: **Climatology response and natural variability.** Zonal mean sea level pressure (SLP) climatology for the Atlantic and the Pacific sectors for a) MPI, b) SPEEDY. Unit: hPa. The Atlantic sector is between $80°W - 0°E$ (blue lines). The Pacific sector is between $130°E - 130°W$ (red lines). Geopotential height composites of 15 to 10 days prior to the onset of weak polar vortex events for c) 1000 hPa MPI RCP8.5 scenario, d) 925 hPa SPEEDY Pac_P experiment, (corresponds to the upward propagating surface anomalies in Fig 3.6c & figure 3.11b). Unit: meters. Regions of 95% statistically significant anomalies are stippled, based on a standard two-sided Student's *t-test*.

From these results, it can be inferred that in the current climate, the stratospheric polar vortex influences the occurrence of AO events (Fig. 3.6a,b), while in a warmer climate that is not the case (Fig. 3.6c); if anything, information flows the opposite direction and the surface AO

could be used to predict the state of the stratospheric vortex.

The high correlation between AO and NAO in the current climate implies that the polar vortex influences both the AO and the NAO equally. A similar analysis is followed to explicitly investigate how the polar vortex influences the NAO. Geopotential height PC time series are calculated independently for each pressure level, except that in this case they are calculated for the NAO domain.

The result shows that, in the reanalysis and in the historical simulations, the weak polar vortex propagates downward to the surface, where a negative NAO appears (see Ayarzagüena et al. (2020), Figs. 3.12a,b & 3.13a,b). Similarly, in RCP8.5, a downward propagation of the signal in the stratosphere is present, and the surface NAO signal coincides with the weak polar vortex onset (Figs. 3.12c & 3.13b). Some weak anomalies are observed in IPSL for the Atlantic sector before the onset of the WPV, due to the extension of the Eurasian high pressure anomalies to the Atlantic as in Fig. 3.10. Thus, there is no indication of the tropospheric signal in the Atlantic preceding that of the stratosphere in the warm climate, as found for the Pacific sector.

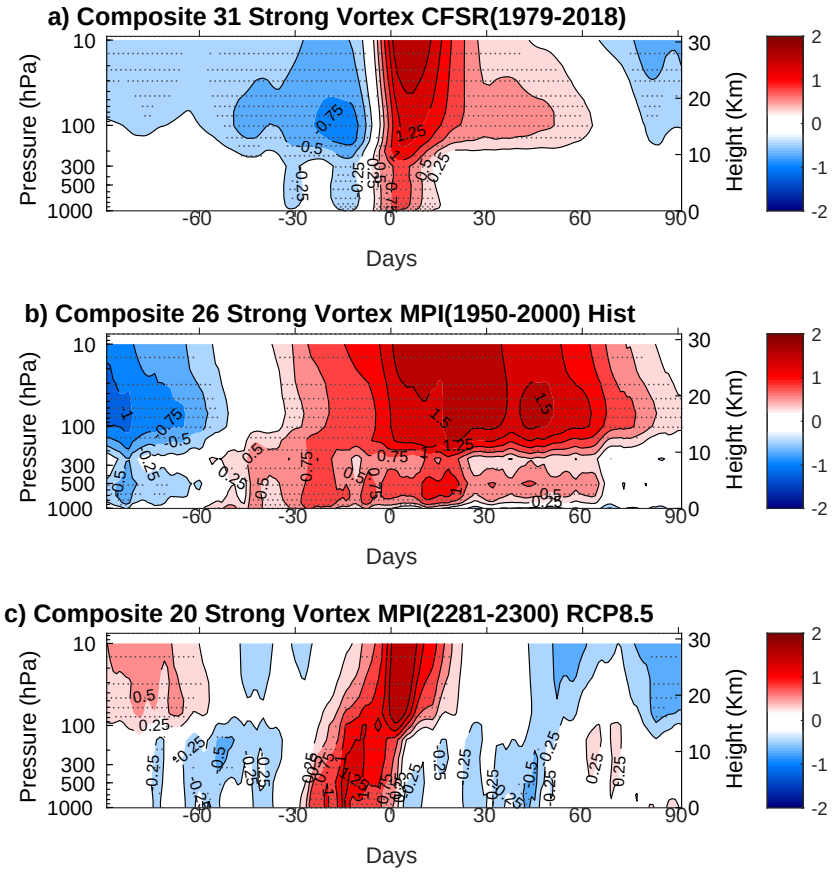

FIGURE 3.8: **Strong Polar Vortex**. a) same as figure 3.6 except that it is for the strong polar vortex (SPV). The condition for a SPV event is when the 10 hPa NAM index is $\geq +1$. Stippling shows the 95% statistically significant anomalies using bootstrapping approach.

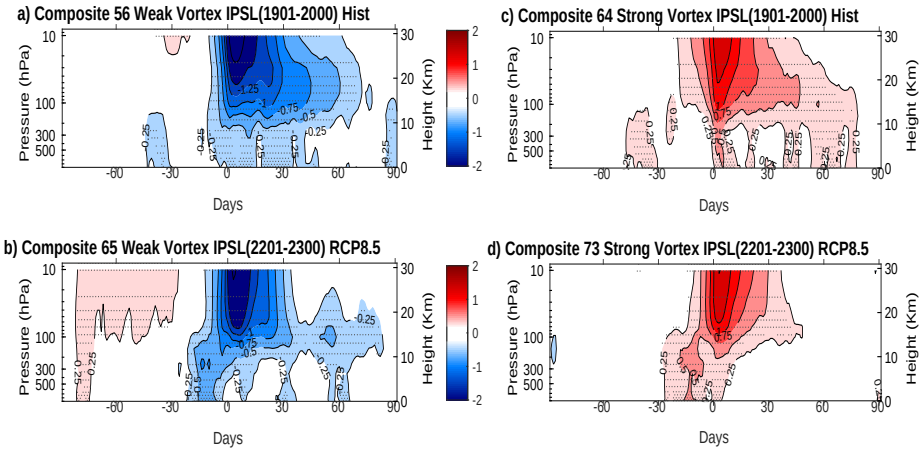

FIGURE 3.9: a) same as figure 3.6 & 3.8, except that it is for IPSL-CM5A-LR.

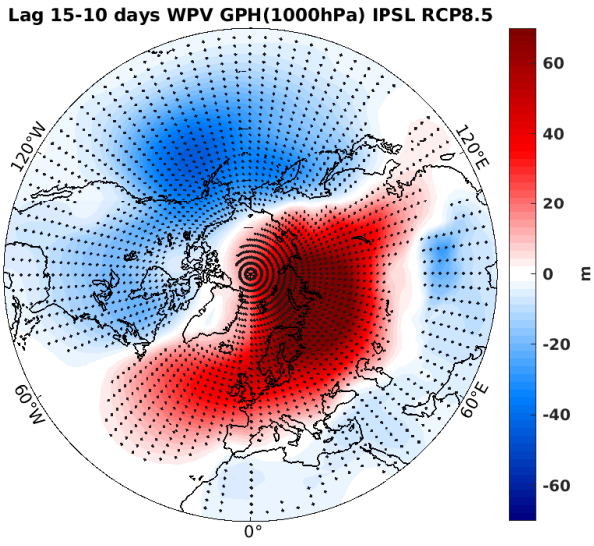

FIGURE 3.10: **Eurasian high and Aleutian low pressure centers leading weak polar vortex.** Same as in fig. 3.7a, except for IPSL-CM5A-LR. (corresponds to the upward propagating surface anomalies in fig 3.9b)

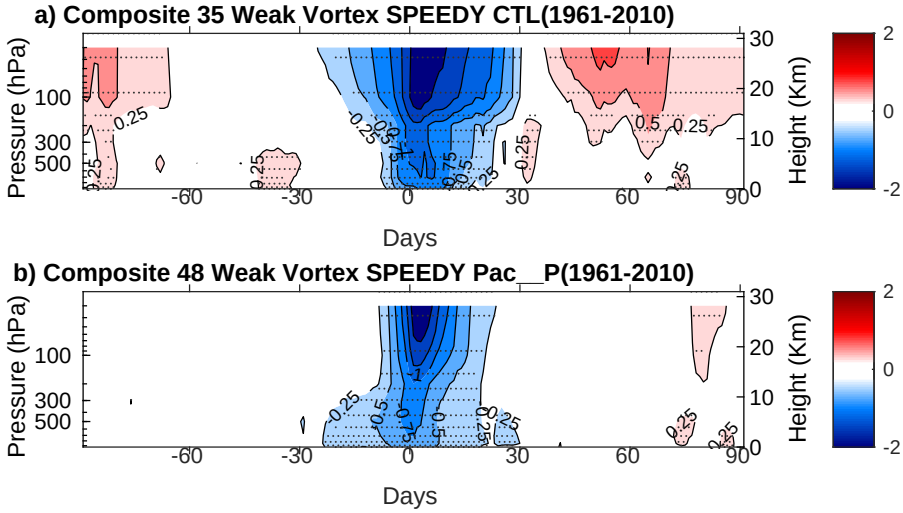

FIGURE 3.11: a) same as figure 3.6, except that it is for SPEEDY AGCM. Note that the condition for the onset is based on NAM index at 30 hPa.

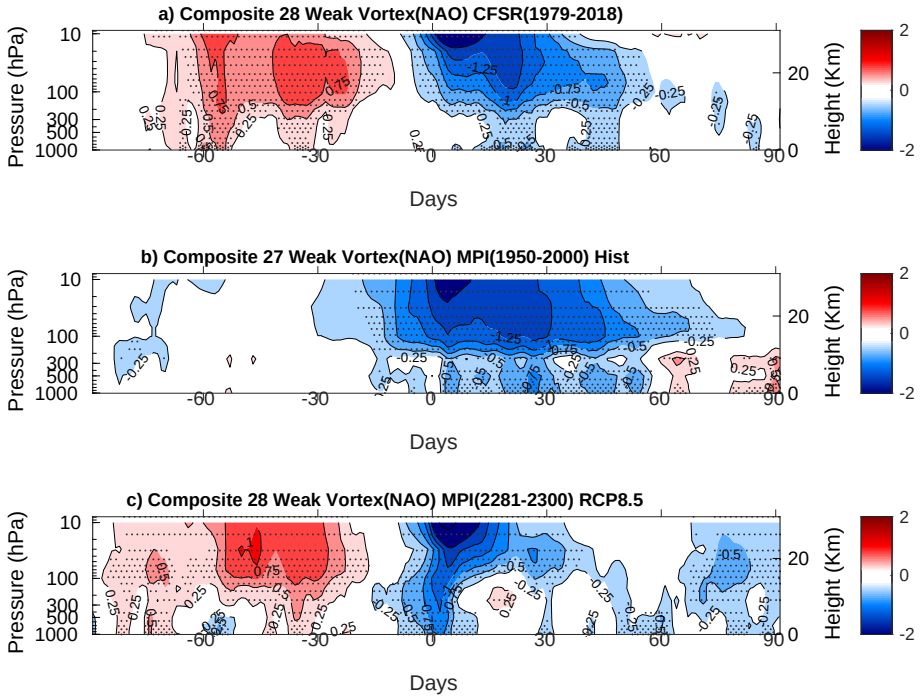

FIGURE 3.12: **Polar vortex influence in the Atlantic sector.** Same as in figure 3.6, except that here NAM index is for NAO domain instead of AO domain. The condition for the onset is still when the 10 hPa NAM index is ≤ -1.5 for weak polar vortex. a) CFSR reanalysis. b) MPI historical. c) MPI RCP8.5. Stippling indicates the 95% statistically significant anomalies using bootstrapping approach.

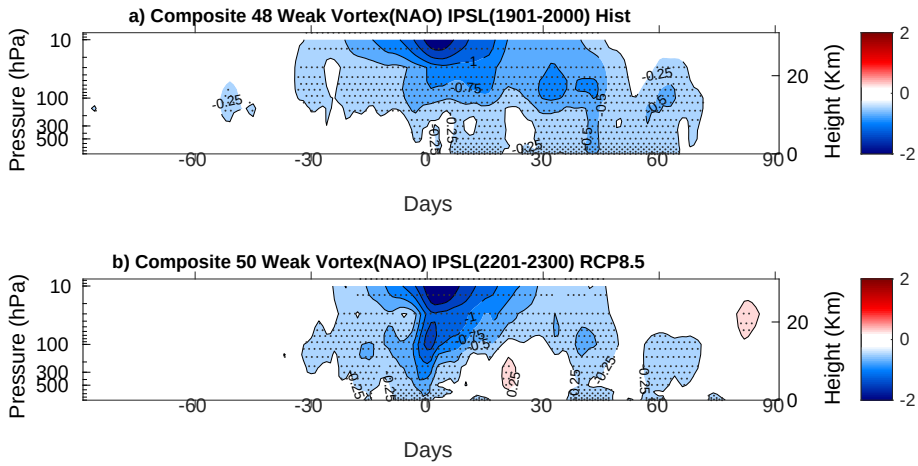

FIGURE 3.13: Same as in 3.12, except for IPSL-CM5A-LR model.

The main limitation of the analysis is that it has been performed on two models only, being the only CMIP5 models for which daily data are available for the RCP8.5 extended runs. These models (MPI-ESM-LR and IPSL-CM5A-LR), however, have a good representation of stratospheric variability (Charlton-Perez et al., 2013), while many other CMIP5 models are known to weakly capture the downward propagation of stratospheric anomalies into the troposphere (Furtado et al., 2015), possibly due to their low vertical resolution near and above the tropopause (Richter, Solomon, and Bacmeister, 2014). Another caution that must be considered is that CMIP5 models are known to have biases in the representation of variability modes in the historical period (Gong et al., 2017), particularly when computing winter seasonal (DJF means) AO variability. Gong et al. (2017) suggests a statistical method for bias correction to cancel out the excess variability in the Pacific region. However, for the purpose of this study, applying a statistical bias correction

that is based on the current climate in order to correct the bias of a different climate is unreasonable. In spite of that, figure 3.14 shows the Arctic Oscillation variability for wintertime mean in both NCEP-CFSR reanalysis and MPI-ESM-LR, showing that the MPI model performs exceptionally well in comparison to reanalysis in this regard, and thus this model has been used here as a preferred model.

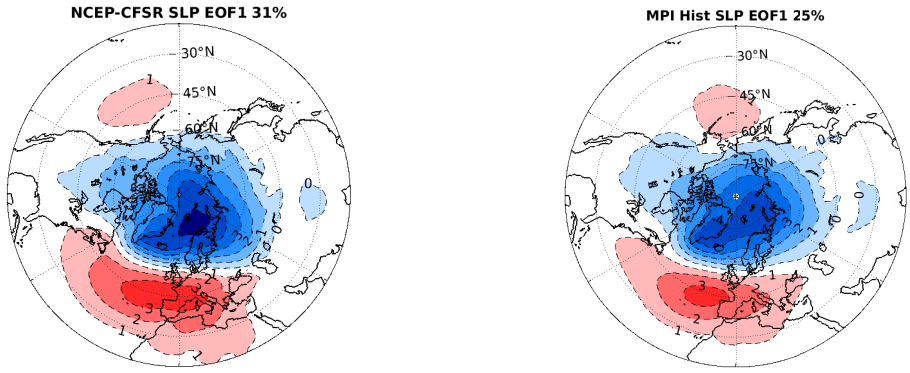

FIGURE 3.14: **The spatial patterns of winter seasonal mean AO**. The leading EOF mode for DJF seasonal mean sea level pressure. The Arctic Oscillation for NCEP-CFSR reanalysis 1979-2018, MPI-ESM-LR 1901-2000. The explained variance by the EOF is indicated on top of each panel. (Contour levels are every 1 *hPa*, corresponding to 1 standard deviation of the PC.)

3.5 The development of NAO events

The coupling between the AO and the NAO as well as the stratosphere-troposphere interactions are shown to be changing under a warmer climate as discussed in the previous sections. Consequently, mid-latitude teleconnections are modified, and are required to be approached in a different way. In this section, a composite analysis is followed to show

the development of NAO events under the light of AO-NAO decoupling.

Figures (3.15,3.16) show composite maps of sea level pressure anomalies prior to and after the onset of negative NAO events in historical and RCP8.5 climate scenarios. NAO events are considered if the NAO PC index is less than -1 and persists for at least 5 consecutive days, and the onset is marked by day 0.

In the historical climate, the negative NAO develops in the Atlantic by forming positive pressure anomalies over Iceland and negative pressure anomalies over the Azores, with a simultaneous development of low pressure anomalies over the north Pacific ocean, showing the influence of the downward propagation of stratospheric polar vortex weakening anomalies. In RCP8.5 climate, a deepening of the Aleutian Low and a strengthening of the Eurasian high precede the development over the Atlantic sector. The seesaw-like pressure anomalies between Eurasia and the north Pacific nudge the stratospheric polar vortex, which is a plausible mechanism by Cohen et al. (2007) in the current climate as well. Afterwards, the weakening of the stratospheric polar vortex handles the forcing of the Atlantic sector to reflect a well-developed negative NAO, while the anomalies over the pacific ocean start to disappear. The timeline of NAO development changes, considering the different nature of stratosphere-troposphere coupling, as shown in figures 3.6, 3.12, 3.13, as it was shown how in the current climate, the stratosphere forces both the Atlantic and the Pacific sectors simultaneously, while in a warmer climate, surface anomalies precede the stratospheric anomalies, and the Atlantic sector is forced thereafter by the stratosphere.

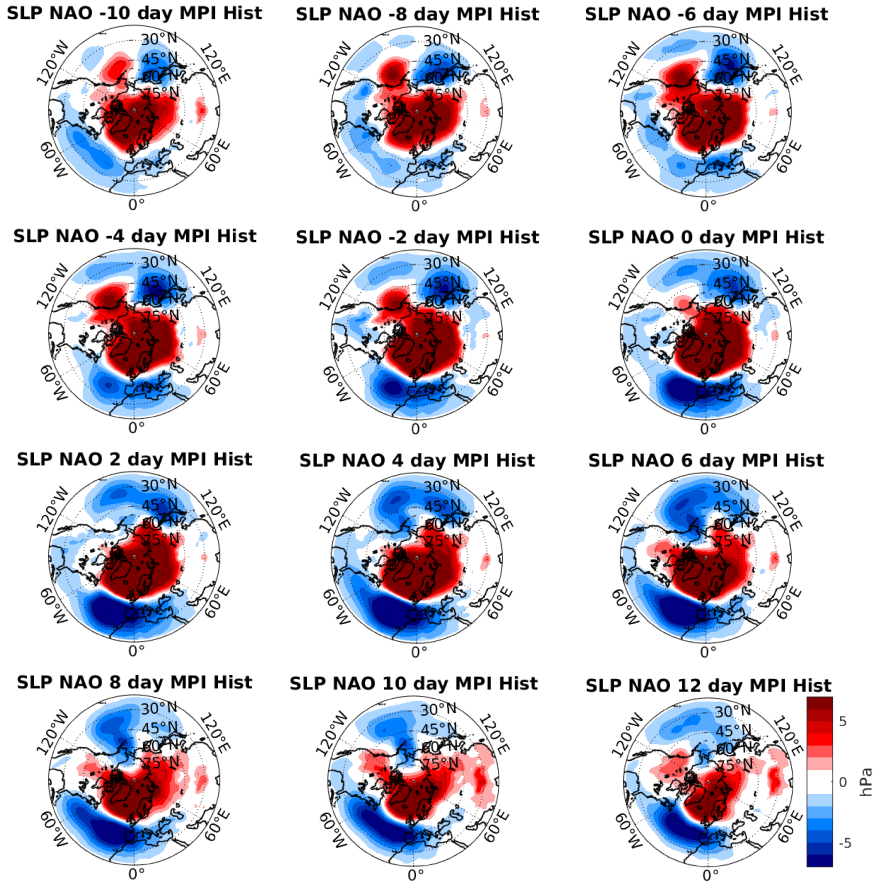

FIGURE 3.15: **The development of NAO events in Historical climate**. Composite maps of sea level pressure anomalies for MPI-ESM-LR model in the historical climate, showing the lag/lead SLP anomalies before/after NAO event. NAO event is considered when the NAO PC index is less than -1, and persists for at least 5 days. (Unit: hPa)

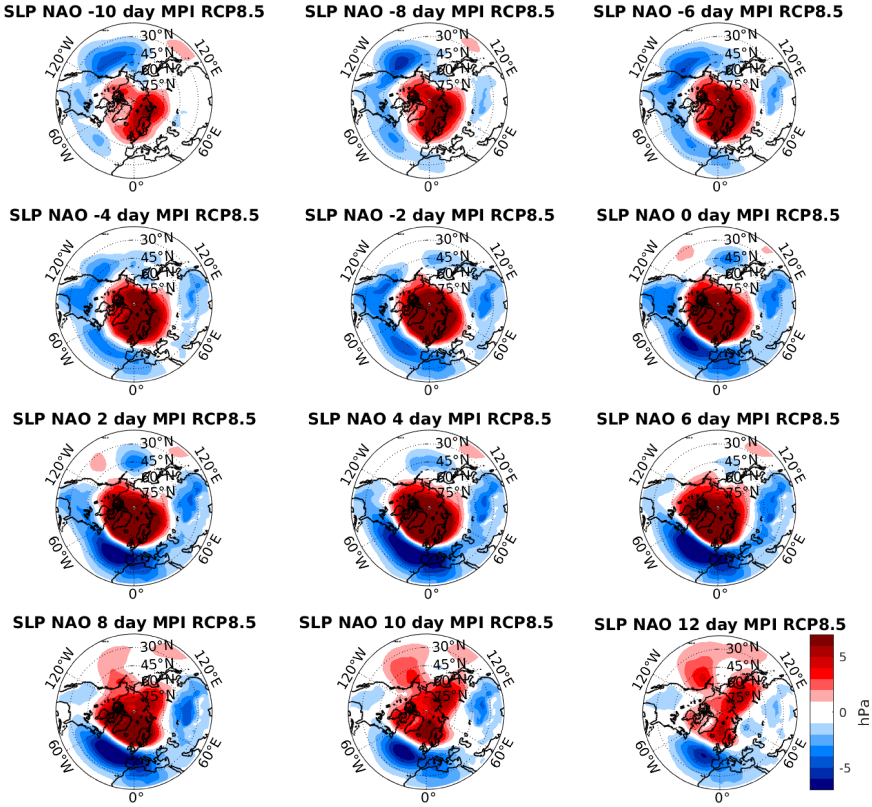

FIGURE 3.16: **The development of NAO events in RCP8.5 climate**. Composite maps of sea level pressure anomalies for MPI-ESM-LR model in the RCP8.5 climate, showing the lag/lead SLP anomalies before/after NAO event. NAO event is considered when the NAO PC index is less than -1, and persists for at least 5 days. (Unit: hPa)

3.6 Land-sea thermal contrast modification

By the 23^{rd} century of RCP8.5 climate scenario, substantial modifications to the current major climatic features occur, such as polar sea ice melting, ocean circulation changes (e.g. AMOC slowdown). In this study, a key feature that is suggested to be important and relevant to

the AO and NAO modes of variability is land-sea thermal contrast. As shown previously in figure 3.4, the rate of warming of the Pacific ocean is much faster than the Atlantic ocean causing the Pacific ocean to become warmer than Atlantic ocean. The differential heating between the two sectors motivates conducting a simple experiment to understand the effect of warming the Pacific as described in section 3.2.5.

Here in this section, the warm up of the Pacific ocean is taken into account from land-sea contrast point of view since it is expected to be modified. Figure 3.17 shows wintertime (DJF) land-sea contrast for the Asian/Pacific front (subtracting regions B minus A in panel a) and the American/Atlantic front (subtracting regions D minus C in panel a) for b) MPI-ESM-LR model Historical and RCP8.5 simulations, and c) SPEEDY climatology control run (CTL) and Pacific perturbation run (Pac_P) as described in section 3.2.5. In the current climate, land-sea contrast in the Pacific is quite comparable to that of the Atlantic as shown for MPI historical and SPEEDY CTL. However, as a consequence of the differential warming in a warmer climate, land-sea temperature contrast becomes larger at the Asian/Pacific front, compared with the American/Atlantic counterpart. Simulating such land-sea contrast change by adding warm SST anomalies over the Pacific using SPEEDY (Pac_P) results in a qualitatively similar modification. However, the Asian/Pacific land-sea thermal contrast does not only increase as a result of warming the Pacific, but rather as result of the development of a dynamical cooling over Asia/Eurasia (figure 3.5b, consistent with Li et al. (2020)). Likewise, the weakening of the American/Atlantic contrast is a consequence of warm air advection over the American continent

that reduces temperature difference between the Atlantic and North America.

Land-sea contrast modification could be a plausible mechanism to explain AO/NAO decoupling since it is shown in the literature that AO variability shifts to the Pacific sector through land-sea contrast modification. This shift is demonstrated by Molteni et al. (2011), where they reduce land-sea contrast in the Northern hemisphere, and show that the AO pattern indeed responds to the reduction. However, the relative difference of land-sea contrast between the Atlantic and the Pacific was not attempted. Here, it was shown (figure 3.1, SPEEDY results in figure 3.2) that the AO mode of variability is sensitive to land-sea thermal contrast modification, causing the Pacific sector to become the preferred region for the covariability with the Arctic in a warmer climate, rather than the Pacific and Atlantic centres of action simultaneously covarying with the Arctic in the current climate.

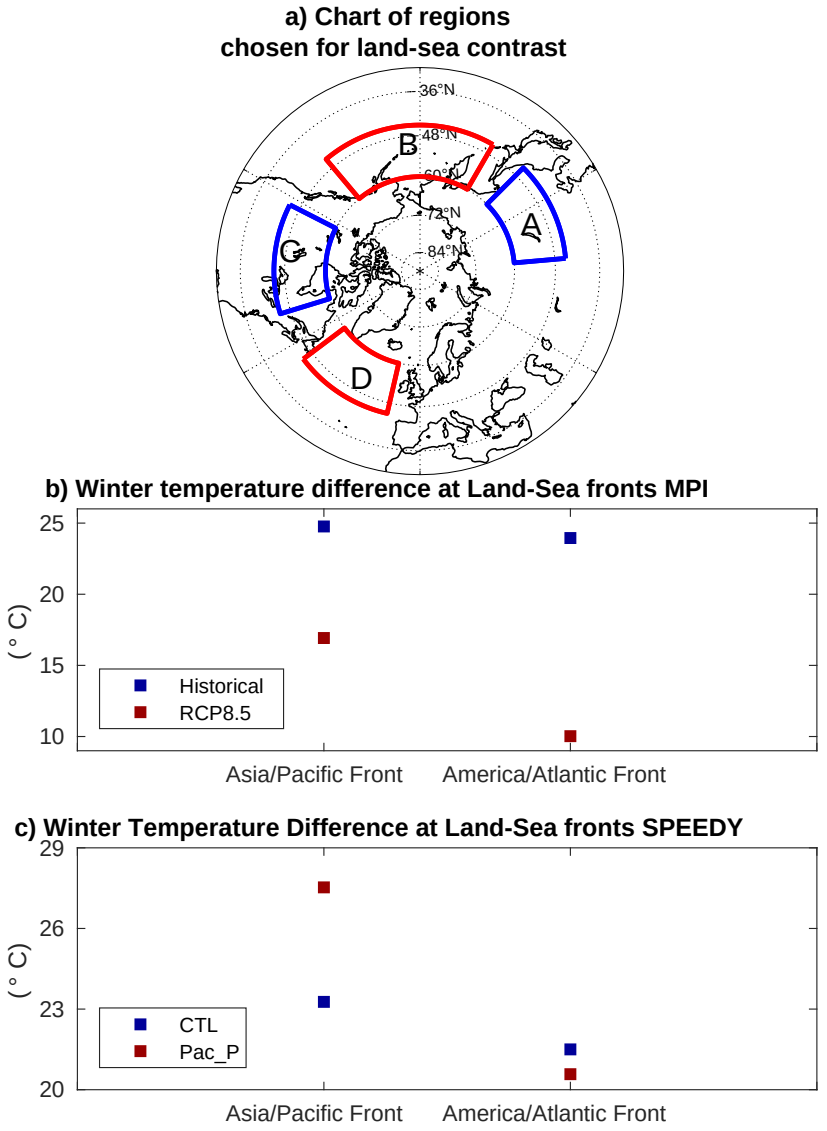

FIGURE 3.17: **Land-sea thermal contrast modification**. a) Regions for which land-sea thermal contrast are calculated in panels (b,c). The differences are calculated by subtracting boxes B minus A for Asia/Pacific front, and boxes D minus C for America/Atlantic front. Winter land-sea thermal contrast at Asia/Pacific and America/Atlantic fronts for b) MPI-ESM-LR and c) SPEEDY simulations. The differences are based on the boxes in panel a. All boxes are bounded by $45°N - 60°N$. A) $95°E - 135°E$. B) $150°E - 140°W$. C) $65°W - 105°W$. D) $55°W - 15°W$

3.7 Further characterization of the response

A change in SST gradients such as that observed in RCP8.5 scenario, or such as the observed in warming up the pacific as in Pac_P experiment is expected to have important consequences on baroclinic activities. In the current climate, the baroclinicity is higher in the Pacific (Nakamura, 1992). It is still not fully understood why the Pacific jet stream becomes weaker in the months when the temperature gradients (baroclinicity) are strongest, and why the Atlantic storm track varies more despite being less baroclinic. In this section, the change of baroclinicity due to the differential warming of the Pacific with respect to the Atlantic is briefly surveyed. As a proxy to demonstrate baroclinicity, Eady growth rate (EGR) is calculated following Hoskins and Valdes (1990):

$$EGR = 0.31\Gamma\frac{f}{N} \tag{3.12}$$

where $\Gamma = \partial U/\partial z$ is the vertical wind shear, f = Coriolis parameter, $N^2 = \frac{g}{\theta}\frac{d\theta}{dz}$ is buoyancy frequency, fU_z is related to the meridional temperature gradient, and N characterizes the vertical stratification of the atmosphere.

Figure 3.18 shows Eady growth rate EGR response for MPI-ESM-LR and SPEEDY experiment. For SPEEDY, the north Pacific SST anomaly causes the meridional temperature gradient to decrease in the most baroclinic region (around $45°N$), therefore, negative EGR anomalies are observed. Intuitively, a region of increased baroclinicity over Bering Strait is observed. This is due to the increased temperature gradient

between the warming region and sea ice over the Arctic. In MPI, the response is more complicated by the absence of sea ice, and temperature gradients between Kuroshio current and the North Pacific (see figure 3.4), and it indicates a poleward shift of the zone of strong baroclinicity. Since a poleward heat flux is necessary for cyclognesis, meridional temperature gradients are important. However, as demonstrated in section 3.6 that zonal temperature gradients are also evident (Land-sea thermal contrast). Therefore, further analysis is required to understand if baroclinicity modifications contribute to AO/NAO decoupling.

A change in baroclinicity (cyclogenesis) directly reflect changes on SLP variability. Figure 3.19 shows zonal sea level pressure standard deviation response over the Atlantic and the Pacific sectors. The variability of SLP changes corresponding to EGR change, where an increase in SLP variability is coincidental with regions of EGR increase.

Tropospheric signals that alter the stratosphere could be depicted in simple deep convection that reaches the tropopause. In RCP8.5, since North Pacific SSTs are substantially higher, convection is likely to be triggered, given approperiate environmental conditions. Figure 3.20 shows a composite of convective precipitation 15 to 10 days prior to polar vortex weakening. However, it is a speculation and further investigation is required.

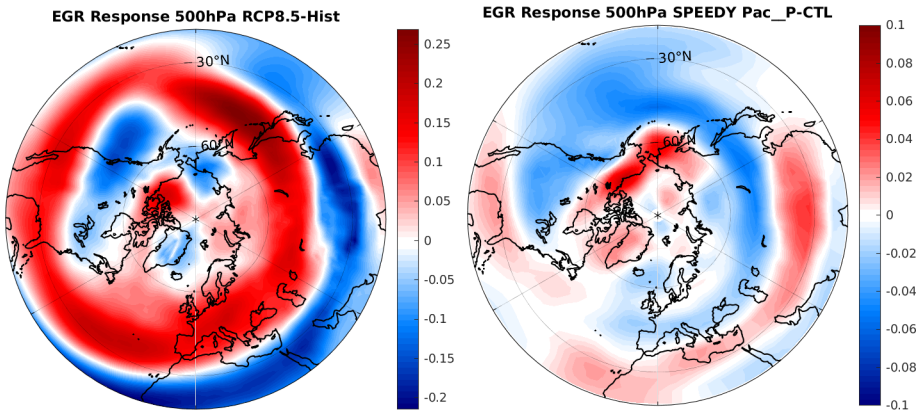

FIGURE 3.18: Eady growth rate response at 500 hPa calculated for MPI-ESM-LR RCP8.5-Hist (left), SPEEDY Pac_P-CTL experiment (right). Unit: 1/day.

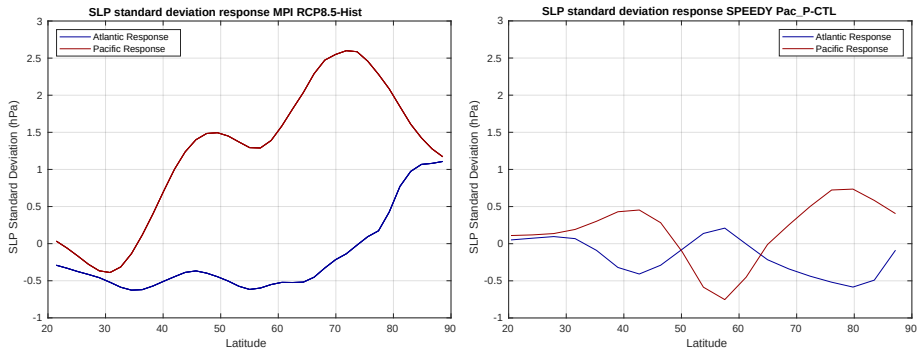

FIGURE 3.19: Response of zonal mean sea level pressure standard deviation over the Pacific and the Atlantic oceans for MPI-ESM-LR RCP8.5-Hist (left), SPEEDY Pac_P-CTL experiment (right). Unit: hPa. Calculated as in figure 3.7(a,b)

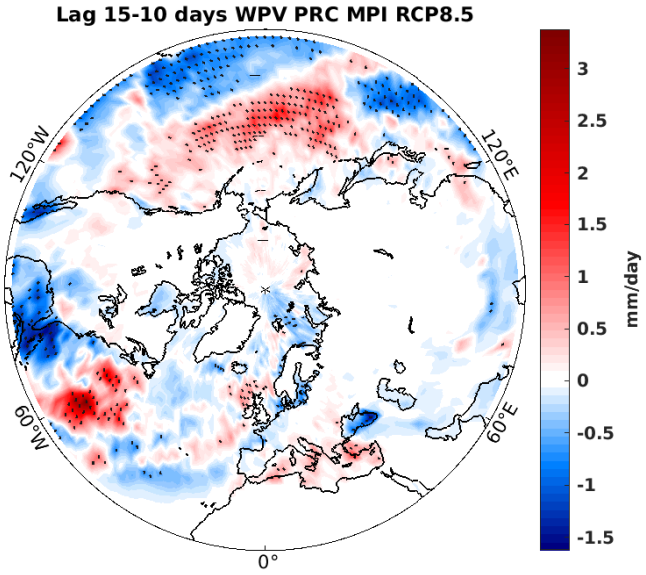

FIGURE 3.20: Composite of convective precipitation 15 to 10 days prior to polar vortex weakening in MPI-ESM-LR RCP8.5. Unit: mm/day. Stippling shows regions of 90% statistically significant anomalies using t-test.

3.8 Polar vortex weakening of December 2020

In closing this chapter, a practical application is worth mentioning in light of the previous findings. As discussed in section 3.1 , the skill of polar vortex prediction in the current climate arises from various climate processes, such as ENSO and QBO in the tropics; Eurasian snow cover and polar sea-ice extent in the high latitudes. In light of this chapter, a new precursor is argued to be useful for predicting the upward propagation of surface anomalies to the stratosphere causing the polar vortex to weaken.

Figure 3.21 shows a composite of sea surface temperature anomalies and sea level pressure anomalies for the first week of December 2020. It is noted that the North Pacific experienced warm anomalies of $3-4°C$, accompanied by negative pressure anomalies in the North Pacific, and high pressure anomalies over Eurasia. SLP pattern can be compared to figures 3.7c obtained in a warm climate, and figure 3.7d that is obtained as a response to a warmer Pacific. The consequence of this SST/SLP setup are consistent with the results of this chapter, as it is illustrated in figure 3.21 that the NAM index indicates surface signal in the first week of December, and propagates upwards to the stratosphere, severely weakening the stratospheric polar vortex within the following 3 weeks. Comparing this particular situation with figure 3.6c and 3.11b, it is argued that a warmer pacific with such surface pressure anomalies setup favor the upward propagation. This arguement does not cross out other possible precursors. Further analysis is needed to confirm such mechanism in the past and upcoming polar vortex events, as a single event is not sufficient. In general, this precursor is likely becoming more relevant in future, as the North Pacific ocean is warming at a higher rate than the North Atlantic, due to the presence of the Atlantic warming hole.

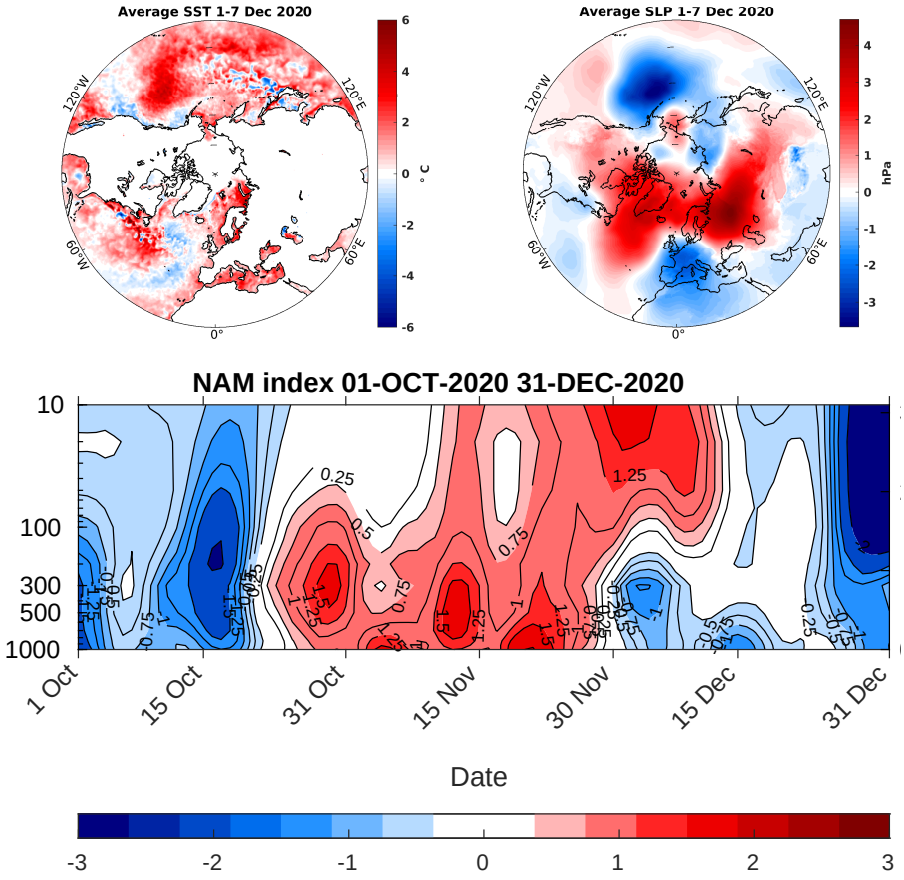

FIGURE 3.21: **Weak polar vortex event of December 2020**. Top left: SST anomalies for the first week in December 2020 with respect to 1979-2010 climatology. Top right: SLP anomalies for the first week in December 2020 with respect to 1979-2010 climatology. Bottom: Time-height development of the NAM index for 1 October till 31 December 2020, obtained with the same method as in section 3.2.4. Data is obtained from ERA5 reanalysis.

Chapter 4

Conclusion

One of the most discussed issues in climate is extreme weather events, since it has a direct impact on society. Whether in winter or in summer, the occurrence of extreme precipitation is an important question that the scientific community strives to address, trying to advance the understanding of the governing processes behind climate extremes. Precipitation in different seasons develop from two different mechanisms. In summer, convection processes leading to mesoscale thunderstorms development, and consequently extreme floods. In winter, large-scale fronts in the mid-latitudes moving across Europe and the North America bringing rainfall from the Pacific and the Atlantic oceans. Moreover, the outbreaks of cold air masses from the Arctic region is an important topic for weather extremes in winter, as polar vortex weakening was responsible for many of weather extreme events over North American and the European continents.

Extreme weather events are studied here through different approaches. Chapter 2 of the study examined different metrics of intense precipitation variability over the European region using different data

products. Gridded observations of daily precipitation (EOBS) indicate that in the 30-year long study period and for all seasons except winter, more regions experienced an increase of extreme precipitation, both in terms of frequency and intensity, than those which recorded a decreasing trend. ERA-Interim reanalysis data, instead, showed an overall decrease in the intense precipitation in all seasons. Higher resolution ERA5 reanalysis showed results that better match those of EOBS, but still reported an overall limited increase in the extreme precipitation especially during the summer season.

The study then investigated the added-value of the dynamical downscaling with a convective-permitting model (WRF on a 4 km grid spacing) on European extreme precipitation frequency and intensity. The defining pattern of extreme precipitation (95th percentile) look consistent in low and high resolution outputs, except for the detailed structure over the mountainous regions of the Great Alpine region. The downscaling shows statistics of extreme precipitation that better match those computed on the gridded observation dataset EOBS. Seasonal trends of frequency of occurrence and intensity of extreme precipitation were shown to be highly dependent on the temporal and spatial resolution for all seasons except for winter.

The overall consistence of all the data products during DJF is related to the fact that extreme winter precipitation in Europe are mainly controlled by the phase of the North Atlantic Oscillation, which is well captured both in low and high resolution runs as it is a large scale process. During the period of the analysis (1979-2008), the North Atlantic

Oscillation went from a period dominated by a negative phase to a period more dominated by a positive phase. The effect of this increase of positive NAO events is reflected in the winter reduction of intense precipitation over Europe, since a positive NAO means that the jet stream flows zonally, and the Arctic air is well confined over the pole. Therefore, the effects of the storms are limited to the northern regions of Europe. Investigation in a different period with a more stable NAO might lead to different results for winter precipitation. There is no evidence of large scale climate modes of variability controlling intense precipitation during the other seasons but more investigations will be necessary to unambiguously attribute the causes of the overall increase of extreme precipitation in Europe.

Since the NAO is known to be trending with global warming based on studies regarding the recent climate change and future warming scenarios, more understanding for the nature of the NAO is necessary. In literature, the North Atlantic Oscillation usually accompanies the Arctic Oscillation as both are highly correlated. Therefore, chapter 3 investigates more in depth how AO and NAO are correlated. An attempt to break the correlation between AO and NAO was performed by examining these modes of variability in an extremely warm climate scenario. This attempt is successful and shows that these patterns are highly dependent on climate mean state.

The decoupling of AO and NAO in a warmer climate shows that the two oscillations are driven by a common driver in the current climate, that is the stratospheric polar vortex, while it was shown that the stratosphere disappears as a common driver for both oscillations in a warmer

climate. In the current climate, the polar vortex (the phase of the Northern Annular Mode) drives surfaces conditions to reflect a certain phase of both AO and NAO. While in a warmer climate, surface conditions over Eurasia and the north Pacific alter the polar vortex, and the polar vortex continues to drive the conditions in the Atlantic sector.

A possible condition for the breakdown between the Arctic and the North Atlantic oscillations is demonstrated. Only warming up the north Pacific ocean led to qualitatively similar results as in a warmer climate. The deepening of the Aleutian low is reproduced in the warm Pacific similar as to what happens in a warmer climate. Moreover, land-sea thermal contrast was discussed as a possible component for the decoupling to occur, since the differential warming in the Pacific and the Atlantic modifies the Asian/Pacific fronts with respect to the American/Atlantic fronts.

Moreover, perturbing the current climate only by warming the north Pacific as in the experiment Pac_P shows the upward propagation of surface anomalies upwards to the stratosphere. It means that the setup of Aleutian/Eurasian surface pressure anomalies, accompanied by warm North Pacific SST anomalies can be used even in the current climate as a precursor for the stratospheric polar vortex.

The breakdown of the connection between the Arctic oscillation and the North Atlantic oscillation in the warm climate projections shows that not only the mean atmospheric circulation changes, but also the modes of variability of the mid to high latitude atmosphere are dramatically modified. The leading hemispheric-EOF (AO) significantly changes in a warmer climate, while the leading regional (Atlantic) EOF

(NAO) is more stable. The results support the fact that these patterns of variability, which are defined to maximize variance, are not some fundamental vibrational mode of the climate system, but patterns that can change in response to changes in the climate. The AO-NAO breakdown is associated with a different connection to the stratospheric variability, which is now recognized as a precursor of the tropospheric signals, while it appears to be triggered by the Pacific and Eurasian surface anomalies in the warm climate.

Bibliography

Alexander, Michael et al. (2018). "Projected sea surface temperatures over the 21st century: Changes in the mean, variability and extremes for large marine ecosystem regions of Northern Oceans". In: *Elem Sci Anth* 6, p. 9. DOI: 10.1525/elementa.191.

Ambaum, Maarten (2010). *Thermal Physics of the Atmosphere (Advancing Weather and Climate Science)*. 1st ed. Wiley. ISBN: 0470745150,9780470745151.

Ambaum, Maarten H. P., Brian J. Hoskins, and David B. Stephenson (2001). "Arctic Oscillation or North Atlantic Oscillation?" In: *Journal of Climate* 14.16, pp. 3495–3507. DOI: 10.1175/1520-0442(2001)014<3495:AOONAO>2.0.CO;2.

Ayarzagüena, Blanca et al. (2020). "Uncertainty in the Response of Sudden Stratospheric Warmings and Stratosphere–Troposphere Coupling to Quadrupled CO2 Concentrations in CMIP6 Models". In: *Journal of Geophysical Research: Atmospheres* 125. DOI: 10.1029/2019JD032345.

Baldwin, M. P. et al. (2001). "The quasi-biennial oscillation". In: *Reviews of Geophysics* 39.2, pp. 179–229. DOI: 10.1029/1999RG000073.

Baldwin, Mark and Timothy Dunkerton (1999). "Propagation of the Arctic Oscillation from the stratosphere to the troposphere". In: *Journal of Geophysical Research: Atmospheres* 104.

Baldwin, Mark P. and Timothy J. Dunkerton (2001). "Stratospheric Harbingers of Anomalous Weather Regimes". In: *Science* 294.5542, pp. 581–584. ISSN: 0036-8075. DOI: 10.1126/science.1063315.

Banerjee, Sudipto and Anindya Roy (2014). "Linear Algebra and Matrix Analysis for Statistics". In.

Bebber, W. van (1891). "Die Zugstraßen der barometrischen Minima nach den Bahnenkarten der Deutschen Seewarte für den Zeitraum 1875-1890". In: *Meteorologische Zeitschrift* 8, 361–366.

Bond, Nicholas A. et al. (2015). "Causes and impacts of the 2014 warm anomaly in the NE Pacific". In: *Geophysical Research Letters* 42.9, pp. 3414–3420.

Bourke, William (1974). "A Multi-Level Spectral Model. I. Formulation and Hemispheric Integrations". In: *Monthly Weather Review* 102.10, pp. 687–701. DOI: 10.1175/1520-0493(1974)102<0687:AMLSMI>2.0.CO;2.

Butler, Amy H. and Lorenzo M. Polvani (2011). "El Niño, La Niña, and stratospheric sudden warmings: A reevaluation in light of the observational record". In: *Geophysical Research Letters* 38.13. DOI: 10.1029/2011GL048084.

Cannon, A. J. and S. Innocenti (2019). "Projected intensification of sub-daily and daily rainfall extremes in convection-permitting climate model simulations over North America: implications for future intensity–duration–frequency curves". In: *Natural Hazards and Earth*

System Sciences 19.2, pp. 421–440. DOI: 10.5194/nhess-19-421-2019. URL: https://nhess.copernicus.org/articles/19/421/2019/.

Casanueva, A. et al. (2014). "Variability of extreme precipitation over Europe and its relationships with teleconnection patterns". In: *Hydrology and Earth System Sciences* 18.2, pp. 709–725. DOI: 10.5194/hess-18-709-2014. URL: https://www.hydrol-earth-syst-sci.net/18/709/2014/.

Charlton-Perez, A. J. et al. (2013). "On the lack of stratospheric dynamical variability in low-top versions of the CMIP5 models". In: *J. Geophys. Res. Atmos.* 118.6, pp. 2494–2505. DOI: 10.1002/jgrd.50125.

Chen, Changlin et al. (2019). "Why Does Global Warming Weaken the Gulf Stream but Intensify the Kuroshio?" In: *Journal of Climate* 32.21, pp. 7437–7451. ISSN: 0894-8755.

Cohen, J. et al. (2007). "Stratosphere-troposphere coupling and links with Eurasian land surface variability". In: *Journal of Climate* 20.21, pp. 5335–5343.

Cohen, Judah and Mathew Barlow (2005). "The NAO, the AO, and Global Warming: How Closely Related?" In: *Journal of Climate* 18.21, pp. 4498–4513. DOI: 10.1175/JCLI3530.1.

Cohen, Judah et al. (2014). "Recent Arctic amplification and extreme mid-latitude weather". In: *Nature Geoscience* 7, pp. 627–637. DOI: 10.1038/ngeo2234.

Coppola, Erika et al. (Dec. 2005). "Bimodality of the North Atlantic Oscillation in simulations with greenhouse gas forcing". In: *Geophysical Research Letters - GEOPHYS RES LETT* 32. DOI: 10.1029/2005GL024080.

Cornes, Richard C. et al. (2018). "An Ensemble Version of the E-OBS Temperature and Precipitation Data Sets". In: *Journal of Geophysical Research: Atmospheres* 123.17, pp. 9391–9409.

Dee, D. P. et al. (2011). "The ERA-Interim reanalysis: configuration and performance of the data assimilation system". In: *Quarterly Journal of the Royal Meteorological Society* 137.656, pp. 553–597. DOI: 10.1002/qj.828.

Dereczynski, Claudine et al. (2020). "Downscaling of climate extremes over South America – Part I: Model evaluation in the reference climate". In: *Weather and Climate Extremes* 29, p. 100273. ISSN: 2212-0947. DOI: https://doi.org/10.1016/j.wace.2020.100273. URL: http://www.sciencedirect.com/science/article/pii/S2212094720300669.

Deser, Clara (2000). "On the teleconnectivity of the "Arctic Oscillation"". In: *Geophysical Research Letters* 27.6, pp. 779–782. DOI: 10.1029/1999GL010945.

Deser, Clara, Robert A. Tomas, and Shiling Peng (2007). "The Transient Atmospheric Circulation Response to North Atlantic SST and Sea Ice Anomalies". In: *Journal of Climate* 20.18, pp. 4751–4767. DOI: 10.1175/JCLI4278.1.

Dufresne, J.-L., M.-A. Foujols, and S. et. al. Denvil (2013). "Climate change projections using the IPSL-CM5 Earth System Model: from CMIP3 to CMIP5". In: *Climate Dynamics* 40.9, pp. 2123–2165. ISSN: 1432-0894. DOI: 10.1007/s00382-012-1636-1.

Eshel, Gidon and Brian Farrell (2001). "Thermodynamics of Eastern Mediterranean Rainfall Variability". In: *Journal of The Atmospheric*

Sciences - J ATMOS SCI 58, pp. 87–92. DOI: 10.1175/1520-0469(2001)058<0087:TOEMRV>2.0.CO;2.

Fischer, Erich and Reto Knutti (Oct. 2016). "Observed heavy precipitation increase confirms theory and early models". In: *Nature Climate Change* 6. DOI: 10.1038/NCLIMATE3110.

Furtado, Jason C. et al. (2015). "Eurasian snow cover variability and links to winter climate in the CMIP5 models". In: *Climate Dynamics* 45.9, pp. 2591–2605. ISSN: 1432-0894. DOI: 10.1007/s00382-015-2494-4.

García-Serrano, J. et al. (2015). "On the Predictability of the Winter Euro-Atlantic Climate: Lagged Influence of Autumn Arctic Sea Ice". In: *Journal of Climate* 28.13, pp. 5195–5216. DOI: 10.1175/JCLI-D-14-00472.1.

Garfinkel, Chaim I et al. (2012). "Observed connection between stratospheric sudden warmings and the Madden-Julian Oscillation". In: *Geophys. Res. Lett.* 39.18, p. L18807. DOI: 10.1029/2012GL053144.

Gent, Peter R. et al. (2011). "The Community Climate System Model Version 4". In: *Journal of Climate* 24.19, pp. 4973–4991. DOI: 10.1175/2011JCLI4083.1.

Gillett, N. P. and J. C. Fyfe (2013). "Annular mode changes in the CMIP5 simulations". In: *Geophysical Research Letters* 40.6, pp. 1189–1193.

Giorgi, F. (2006). "Climate change hot-spots". In: *Geophysical Research Letters* 33.8.

Giorgi, Filippo et al. (July 2016). "Enhanced summer convective rainfall at Alpine high elevations in response to climate warming". In: *Nature Geoscience* 9. DOI: 10.1038/ngeo2761.

Gong, Hainan et al. (2017). "Biases of the wintertime Arctic Oscillation in CMIP5 models". In: *Environmental Research Letters* 12, p. 014001. DOI: 10.1088/1748-9326/12/1/014001.

Goodess, C. M. and P. D. Jones (2002). "Links between circulation and changes in the characteristics of Iberian rainfall". In: *International Journal of Climatology* 22.13, pp. 1593–1615. DOI: 10.1002/joc.810.

Gueremy, J.-F, Nabil Laanaia, and J.-P Ceron (July 2012). "Seasonal forecast of French Mediterranean heavy precipitating events linked to weather regimes". In: *Natural Hazards and Earth System Sciences* 12, pp. 2389–2398. DOI: 10.5194/nhess-12-2389-2012.

Hartman, D.L. et al. (2013). "Observations: Atmosphere and Surface". In: *Climate change 2013 the physical science basis: Working group I contribution to the fifth assessment report of the intergovernmental panel on climate change*. Cambridge University Press, pp. 159–254.

Held, Isaac M. and Max J. Suarez (1994). "A Proposal for the Intercomparison of the Dynamical Cores of Atmospheric General Circulation Models". In: *Bulletin of the American Meteorological Society* 75.10, pp. 1825–1830. DOI: 10.1175/1520-0477(1994)075<1825:APFTIO>2.0.CO;2.

Hersbach, Hans et al. (2020). "The ERA5 global reanalysis". In: *Quarterly Journal of the Royal Meteorological Society* 146.730, pp. 1999–2049.

Hodnebrog, Ø et al. (2019). "Intensification of summer precipitation with shorter time-scales in Europe". In: *Environmental Research Letters* 14.12, p. 124050. DOI: 10.1088/1748-9326/ab549c.

Holland, Marika M. (2003). "The North Atlantic Oscillation–Arctic Oscillation in the CCSM2 and Its Influence on Arctic Climate Variability". In: *Journal of Climate* 16.16, pp. 2767–2781. DOI: 10.1175/1520-0442(2003)016<2767:TNAOOI>2.0.CO;2.

Holton, James R. (2013). *An Introduction to Dynamic Meteorology*. Academic Press.

Hoskins, Brian and Paul Valdes (Aug. 1990). "On the Existence of Storm-Tracks". In: *Journal of The Atmospheric Sciences - J ATMOS SCI* 47, pp. 1854–1864.

Hosseinzadehtalaei, Parisa, Hossein Tabari, and Patrick Willems (2020). "Climate change impact on short-duration extreme precipitation and intensity–duration–frequency curves over Europe". In: *Journal of Hydrology* 590, p. 125249. ISSN: 0022-1694. DOI: https://doi.org/10.1016/j.jhydrol.2020.125249. URL: http://www.sciencedirect.com/science/article/pii/S0022169420307095.

Huang, Danqing et al. (Feb. 2017). "Uncertainty of global summer precipitation in the CMIP5 models: a comparison between high-resolution and low-resolution models". In: *Theoretical and Applied Climatology*. DOI: 10.1007/s00704-017-2078-9.

Hurrell, James W. (1995). "Decadal Trends in the North Atlantic Oscillation: Regional Temperatures and Precipitation". In: *Science* 269.5224, pp. 676–679. ISSN: 0036-8075. DOI: 10.1126/science.269.5224.676.

Hurrell, James W. and Clara Deser (2009). "North Atlantic climate variability: The role of the North Atlantic Oscillation". In: *Journal of Marine Systems* 78.1, pp. 28 –41. ISSN: 0924-7963.

Husak, Gregory J., Joel Michaelsen, and Chris Funk (2007). "Use of the gamma distribution to represent monthly rainfall in Africa for drought monitoring applications". In: *International Journal of Climatology* 27.7, pp. 935–944. DOI: 10.1002/joc.1441.

IPCC (2000). "Emissions scenarios - special report of the Intergovernmental Panel on Climate Change". In: *Intergovernmental Panel on Climate Change, 599 pp., Cambridge Univ. Press, New York.*

— (2013). "Summary for Policymakers". In: *Climate Change 2013: The Physical Science Basis. Contribution of Working Group I to the Fifth Assessment Report of the Intergovernmental Panel on Climate Change*. Ed. by T.F. Stocker et al. Cambridge, United Kingdom and New York, NY, USA: Cambridge University Press. Chap. SPM, 1–30. ISBN: ISBN 978-1-107-66182-0. DOI: 10.1017/CBO9781107415324.004. URL: www.climatechange2013.org.

James, P. et al. (2004). "Climatological aspects of the extreme European rainfall of August 2002 and a trajectory method for estimating the associated evaporative source regions". In: *Natural Hazards and Earth System Sciences* 4.5/6, pp. 733–746.

Jiang, Zhina, Steven B. Feldstein, and Sukyoung Lee (2017). "The relationship between the Madden–Julian Oscillation and the North Atlantic Oscillation". In: *Quarterly Journal of the Royal Meteorological Society* 143.702, pp. 240–250. DOI: 10.1002/qj.2917.

Johns, T. C. et al. (2006). "The New Hadley Centre Climate Model (HadGEM1): Evaluation of Coupled Simulations". In: *Journal of Climate* 19.7, pp. 1327–1353. DOI: 10.1175/JCLI3712.1.

Jones, Philip W. (Sept. 1999). "First- and Second-Order Conservative Remapping Schemes for Grids in Spherical Coordinates". In: *Monthly Weather Review* 127.9, pp. 2204–2210.

Kang, W. and E. Tziperman (2017). "More frequent Sudden Stratospheric Warming events due to enhanced MJO forcing expected in a warmer climate". In: *Journal of Climate* 30.21, pp. 8727–8743.

Kendon, Elizabeth et al. (June 2014). "Heavier summer downpours with climate change revealed by weather forecast resolution model". In: *Nature Climate Change* 4, pp. 570–576. DOI: 10.1038/nclimate2258.

Kretschmer, Marlene et al. (2016). "Using Causal Effect Networks to Analyze Different Arctic Drivers of Midlatitude Winter Circulation". In: *Journal of Climate* 29.11, pp. 4069–4081. DOI: 10.1175/JCLI-D-15-0654.1.

Kucharski, F. and F. Molteni (2003). "On non-linearities in a forced North Atlantic Oscillation". In: *Climate Dynamics* 21.7, pp. 677–687. ISSN: 1432-0894. DOI: 10.1007/s00382-003-0347-z.

Kucharski, F., F. Molteni, and A. Bracco (2006a). "Decadal interactions between the western tropical Pacific and the North Atlantic Oscillation". In: *Climate Dynamics* 26.1, pp. 79–91.

Kucharski, F. et al. (2013). "On the Need of Intermediate Complexity General Circulation Models: A "SPEEDY" Example". In: *Bulletin of the American Meteorological Society* 94.1, pp. 25–30. DOI: 10.1175/BAMS-D-11-00238.1.

Lawrence, Zachary D. et al. (2020). "The Remarkably Strong Arctic Stratospheric Polar Vortex of Winter 2020: Links to Record-Breaking

Arctic Oscillation and Ozone Loss". In: *Journal of Geophysical Research: Atmospheres* 125.22, e2020JD033271. DOI: https://doi.org/10.1029/2020JD033271.

Leeuw, J., John Methven, and M. Blackburn (June 2014). "Evaluation of ERA-Interim reanalysis precipitation products using England and Wales observations". In: *Quarterly Journal of the Royal Meteorological Society* 141. DOI: 10.1002/qj.2395.

Lenderink, Geert and Erik van Meijgaard (2010). "Linking increases in hourly precipitation extremes to atmospheric temperature and moisture changes". In: *Environmental Research Letters* 5.2, p. 025208.

Li, Baofu et al. (2020). "Recent fall Eurasian cooling linked to North Pacific sea surface temperatures and a strengthening Siberian high". In: *Nature Communications* 11. DOI: 10.1038/s41467-020-19014-2.

Lohmann Felix Lüönd, Fabian Mahrt (2016). *An Introduction to Clouds: From the Microscale to Climate*. 1st ed. Cambridge University Press.

Lutgens, F. K. and E. K. Tarbuck (2016). *The atmosphere: an introduction to meteorology*. 13th ed. Pearson. ISBN: 0321984625.

Mishra, Vimal, John M. Wallace, and Dennis P. Lettenmaier (2012). "Relationship between hourly extreme precipitation and local air temperature in the United States". In: *Geophysical Research Letters* 39.16.

Molteni, F. (2003). "Atmospheric simulations using a GCM with simplified physical parameterizations. I: model climatology and variability in multi-decadal experiments". In: *Climate Dynamics* 20.2, pp. 175–191.

Molteni, Franco et al. (2011). "Planetary-scale variability in the northern winter and the impact of land–sea thermal contrast". In: *Climate Dynamics* 37, pp. 151–170. DOI: 10.1007/s00382-010-0906-z.

Myhre, Gunnar et al. (Nov. 2019). "Frequency of extreme precipitation increases extensively with event rareness under global warming". In: *Scientific Reports* 9, p. 16063. DOI: 10.1038/s41598-019-52277-4.

Nakamura, Hisashi (Aug. 1992). "Midwinter Suppression of Baroclinic Wave Activity in the Pacific". In: *Journal of Atmospheric Sciences* 49, pp. 1629–1642.

Nakamura, Tetsu et al. (2016). "The stratospheric pathway for Arctic impacts on midlatitude climate". In: *Geophysical Research Letters* 43.7, pp. 3494–3501. DOI: 10.1002/2016GL068330.

North, Gerald et al. (1982). "Sampling Errors in the Estimation of Empirical Orthogonal Functions". In: *Monthly Weather Review* 110. DOI: 10.1175/1520-0493(1982)110<0699:SEITEO>2.0.CO;2.

Overland, James et al. (2020). "The Polar Vortex and Extreme Weather: The Beast from the East in Winter 2018". In: *Atmosphere* 11, p. 664. DOI: 10.3390/atmos11060664.

Papalexiou, Simon Michael and Alberto Montanari (2019). "Global and Regional Increase of Precipitation Extremes Under Global Warming". In: *Water Resources Research* 55.6, pp. 4901–4914.

Peings, Yannick and Gudrun Magnusdottir (2014). "Response of the Wintertime Northern Hemisphere Atmospheric Circulation to Current and Projected Arctic Sea Ice Decline: A Numerical Study with CAM5". In: *Journal of Climate* 27.1, pp. 244–264. DOI: 10.1175/JCLI-D-13-00272.1.

Peixoto, J P and A H Oort (1992). "Physics of climate". In: URL: https://www.osti.gov/biblio/7287064.

Pieri, Alexandre B. et al. (July 2015). "Sensitivity of Precipitation Statistics to Resolution, Microphysics, and Convective Parameterization: A Case Study with the High-Resolution WRF Climate Model over Europe". In: *Journal of Hydrometeorology* 16.4, pp. 1857–1872.

Pinto, Joaquim G. and Christoph C. Raible (2012). "Past and recent changes in the North Atlantic oscillation". In: *WIREs Climate Change* 3.1, pp. 79–90. DOI: 10.1002/wcc.150.

Polvani, L. M. and R. Saravanan (2000). "The Three-Dimensional Structure of Breaking Rossby Waves in the Polar Wintertime Stratosphere". In: *Journal of the Atmospheric Sciences* 57.21, pp. 3663–3685. DOI: 10.1175/1520-0469(2000)057<3663:TTDSOB>2.0.CO;2.

Raddatz, Thomas et al. (2007). "Will the tropical land biosphere dominate the climate–carbon cycle feedback during the twenty-first century?." In: *Climate Dynamics* 29, pp. 565–574. DOI: 10.1007/s00382-007-0247-8.

Rahmstorf, Stefan et al. (2015). "Exceptional twentieth-Century slowdown in Atlantic Ocean overturning circulation". In: *Nature Climate Change* 5. DOI: 10.1038/nclimate2554.

Rayner, N. A. et al. (2003). "Global analyses of sea surface temperature, sea ice, and night marine air temperature since the late nineteenth century". In: *Journal of Geophysical Research: Atmospheres* 108.D14.

Richter, Jadwiga H., Abraham Solomon, and Julio T. Bacmeister (2014). "Effects of vertical resolution and nonorographic gravity wave drag

on the simulated climate in the Community Atmosphere Model, version 5". In: *Journal of Advances in Modeling Earth Systems* 6.2, pp. 357–383. DOI: 10.1002/2013MS000303.

Ruggieri, P. et al. (2017). "The transient atmospheric response to a reduction of sea-ice cover in the Barents and Kara Seas". In: *Quarterly Journal of the Royal Meteorological Society* 143.704, pp. 1632–1640. DOI: 10.1002/qj.3034.

Saha, Suranjana et al. (2010). "The NCEP climate forecast system reanalysis". In: *Bulletin of The American Meteorological Society - BULL AMER METEOROL SOC* 91. DOI: 10.1175/2010BAMS3001.1.

Santos, Mónica et al. (Oct. 2018). "Recent and future changes of precipitation extremes in mainland Portugal". In: *Theoretical and Applied Climatology*. DOI: 10.1007/s00704-018-2667-2.

Scaife, Adam et al. (Jan. 2008). "European climate extremes and the North Atlantic Oscillation". In: *Journal of Climate* 21, pp. 72–83.

Schmidt, Gavin A. et al. (2014). "Configuration and assessment of the GISS ModelE2 contributions to the CMIP5 archive". In: *Journal of Advances in Modeling Earth Systems* 6.1, pp. 141–184. DOI: 10.1002/2013MS000265.

Seneviratne, Sonia et al. (Apr. 2012). "Changes in climate extremes and their impacts on the natural physical environment: An overview of the IPCC SREX report". In: pp. 12566–.

Skok, Gregor et al. (Jan. 2015). "Precipitation intercomparison of a set of satellite- and raingauge-derived datasets, ERA Interim reanalysis, and a single WRF regional climate simulation over Europe and the

North Atlantic". In: *Theoretical and Applied Climatology* 123. DOI: 10.1007/s00704-014-1350-5.

Stohl, Andreas and Paul James (Dec. 2005). "A Lagrangian Analysis of the Atmospheric Branch of the Global Water Cycle. Part II: Moisture Transports between Earth's Ocean Basins and River Catchments". In: *Journal of Hydrometeorology* 6.6, pp. 961–984.

Sévellec, Florian, Alexey Fedorov, and Wei Liu (2017). "Arctic sea-ice decline weakens the Atlantic Meridional Overturning Circulation". In: *Nature Climate Change* 7. DOI: 10.1038/nclimate3353.

Taylor Saïd, Lebel (1997). "Interactions between the Land Surface and Mesoscale Rainfall Variability during HAPEX-Sahel". In: *Monthly Weather Review* 125.9, pp. 2211 –2227. DOI: 10.1175/1520-0493(1997)125<2211:IBTLSA>2.0.CO;2.

Thompson, David W. J. and John M. Wallace (1998). "The Arctic oscillation signature in the wintertime geopotential height and temperature fields". In: *Geophysical Research Letters* 25.9, pp. 1297–1300. DOI: 10.1029/98GL00950.

Thompson, David W. J., John M. Wallace, and Gabriele C. Hegerl (2000). "Annular Modes in the Extratropical Circulation. Part II: Trends". In: *Journal of Climate* 13.5, pp. 1018–1036. DOI: 10.1175/1520-0442(2000)013<1018:AMITEC>2.0.CO;2.

Thompson, D.W.J. and J.M. Wallace (2000). "Annular modes in the extratropical circulation. Part I: Month-to-month variability". In: *Journal of Climate* 13, pp. 1000–1016. DOI: 10.1175/1520-0442(2000)01360;1000:amitec62;2.0.co;2.

Totz, Sonja et al. (2017). "Winter Precipitation Forecast in the European and Mediterranean Regions Using Cluster Analysis". In: *Geophysical Research Letters* 44.24, pp. 12,418–12,426.

Trenberth, K.E. and Simon Josey (Jan. 2007). "Observations: surface and atmospheric climate change". In.

Trenberth, Kevin (Mar. 2011). "Changes in Precipitation with Climate Change. Climate Change Research". In: *Climate Research* 47, pp. 123–138. DOI: 10.3354/cr00953.

Voldoire, A., E. Sanchez-Gomez, and D. et. al Salas y Mélia (2013). "The CNRM-CM5.1 global climate model description and basic evaluation". In: *Climate Dynamics* 40.9, pp. 2091–2121. ISSN: 1432-0894. DOI: 10.1007/s00382-011-1259-y.

Volosciuk, Claudia et al. (Aug. 2016). "Rising Mediterranean Sea Surface Temperatures Amplify Extreme Summer Precipitation in Central Europe". In: *Scientific Reports* 6, p. 32450. DOI: 10.1038/srep32450.

Walker, G. T. and E. W. Bliss (1932). "World weather". In: *V. Mem. Roy. Meteor. Soc.* 4, pp. 53–84.

Wanner, Heinz et al. (2001). "North Atlantic Oscillation – Concepts And Studies". In: *Surveys in Geophysics* 22.4, pp. 321–381. DOI: 10.1023/A:1014217317898.

Wu, Qigang and Xiangdong Zhang (2010). "Observed forcing-feedback processes between Northern Hemisphere atmospheric circulation and Arctic sea ice coverage". In: *Journal of Geophysical Research: Atmospheres* 115.D14. DOI: 10.1029/2009JD013574.

Zolina, Olga et al. (July 2005). "On the robustness of the estimates of centennial-scale variability in heavy precipitation from station data

over Europe". In: *Geophysical Research Letters* 32. DOI: 10.1029/2005GL023231.

Zolina, Olga et al. (2008). "Seasonally dependent changes of precipitation extremes over Germany since 1950 from a very dense observational network". In: *Journal of Geophysical Research: Atmospheres* 113.D6. DOI: 10.1029/2007JD008393.

Zolina, Olga et al. (June 2009). "Improving Estimates of Heavy and Extreme Precipitation Using Daily Records from European Rain Gauges". In: *Journal of Hydrometeorology* 10. DOI: 10.1175/2008JHM1055.1.